A Novel 3-Way Dual-Band Doherty Power Amplifier for Enhanced Concurrent Operation

Ruwaybih Alsulami, *Student Member, IEEE*, Patrick Roblin, *Senior Member, IEEE*, Jose I. Martinez-Lopez, *Member, IEEE*, Yunsik Hahn, *Student Member, IEEE*, Chenyu Liang, *Member, IEEE*, Zoya Popovic, *Fellow, IEEE*, and Vanessa Chen, *Member, IEEE*

***Abstract*— This article presents the architecture and design methodology for a new type of dual-band Doherty power amplifier (DB-DPA), referred to as 3-Way DB-DPA, which consists of a main amplifier for each band and an auxiliary amplifier handling both bands. The 3-Way DB-DPA improves the average drain efficiency in concurrent dual-band operation compared to the traditional 2-Way DB-DPA, by avoiding early clipping in the main amplifiers, while benefiting from load—pulling from the auxiliary power amplifier (PA). This improvement is verified in theory and simulation at the current-source reference planes and in measurement with a fabricated 1.5- and 2-GHz dual-band PA. A statistical analysis using 2-D continuous-wave (CW) signals with long-term evolution (LTE) probability distribution functions (PDFs) is performed and demonstrated an improvement in the concurrent average efficiency by 15 percentage points compared to the conventional 2-Way DB-DPA. In nonconcurrent operation, the measured CW drain efficiency in the lower band (1.5 GHz) is 82.8% at peak and 66.6% at 9.6-dB backoff, and the measured CW drain efficiency in the upper band (2.0 GHz) is 70.0% at peak and 48.4% at 9.4-dB backoff. The CW concurrent-balanced drain efficiency reaches 66.2/52.0% in the 3-Way DB-DPA at 3-/6-dB backoff. In single-band operation at 1.5/2.0 GHz, the average power and average drain efficiency after linearization by digital predistortion (DPD) are 35.1/37.4 dBm and 65.0/53.7%, respectively, for an LTE signal with 10-MHz bandwidth and 6.1-dB peak-to-average power ratio (PAPR). In concurrent operation, the 3-Way DB-DPA is driven by two 10-MHz LTE uncorrelated signals at 1.5 GHz with 6.86-dB PAPR and at 2.0 GHz with 6.26-dB PAPR, and the average total power and average concurrent drain efficiency after DPD are 37.5 dBm and 54.24%, respectively.**

***Index Terms*— Concurrent average efficiency, Doherty power amplifier (DPA), dual band, intermodulation (IM), 3-Way DB-DPA, 2-D digital predistortion (DPD).**

WITH the rapid growth in modern communication, transmitter systems must use a wider fraction of the spectrum, to support the continuously increasing data rate. In addition, signals with large peak-to-average power ratio (PAPR) are used in communication systems to increase the spectral efficiency. This has led to an increased demand for multiband and broadband power amplifiers (PAs) for signals with large PAPR.

The PA is one of the most power-consuming components in the transmitter system, and this is why it is important to achieve high average power efficiency, for signals with large PAPR. Therefore, the Doherty PA is widely used because it exhibits a high efficiency over an extended backoff power range [1]–[3]. The Doherty power amplifier (DPA) was invented by William H. Doherty in 1936 at Bell Telephone Laboratories. Doherty [1] described the DPA in his own words as "A New High-Efficiency Power Amplifier for Modulated Waves." For single-band (SB) operation, the DPA has been studied extensively, and it has been shown that it can achieve high average efficiency for signals with large PAPR [4]–[7]. For the multiband operation mode, the conventional DPA faces significant challenges to achieve high average efficiency. The first realization of a dual-band DPA (DB-DPA) was reported by Colantonio *et al.* [8]. In recent years, efforts have been made to improve the average efficiency by introducing new design techniques and methodologies, such as frequency-dependent backoff power ranges [9], precise impedance terminations [10], a modified Π-network at the output combiner [11], a dual-band T-network impedance transformer [12], intermodulation (IM) impedance tuning [13], novel dual-band typologies [14], frequency-dependent input power division [15], three-stage DB-DPA [16], and direct impedance matching transformation [17]. As a result, the drain

Manuscript received January 29, 2021; revised March 31, 2021 and May 2, 2021; accepted May 7, 2021. The work of Ruwaybih Alsulami was supported by Umm Al Qura University in coordination with the Ministry of Higher Education, Saudi Arabia. The work of Patrick Roblin and Vanessa Chen was supported in part by NSF under Grant 1952907. The work of Jose I. Martinez-Lopez was supported by the Programa de Apoyos para la Superación del Personal Académico de la UNAM (DGAPA-PASPA). *(Corresponding author: Patrick Roblin.)*

Ruwaybih Alsulami, Patrick Roblin, Yunsik Hahn, and Chenyu Liang are with the Department of Electrical and Computer Engineering, The Ohio State University, Columbus, OH 43210 USA (e-mail: roblin.1@osu.edu).

Jose I. Martinez-Lopez is with the Department of Electrical and Computer Engineering, The Ohio State University, Columbus, OH 43210 USA, and also with the Division de Ingenieria Electrica, Universidad Nacional Autonoma de Mexico, Mexico City 04150, Mexico.

Zoya Popovic is with the Department of Electrical, Computer and Energy Engineering, University of Colorado at Boulder, Boulder, CO 80309 USA.

Vanessa Chen is with the Department of Electrical and Computer Engineering, Carnegie Mellon University, PA 15213 USA.

Color versions of one or more figures in this article are available at https://doi.org/10.1109/TMTT.2021.3091507.

Digital Object Identifier 10.1109/TMTT.2021.3091507

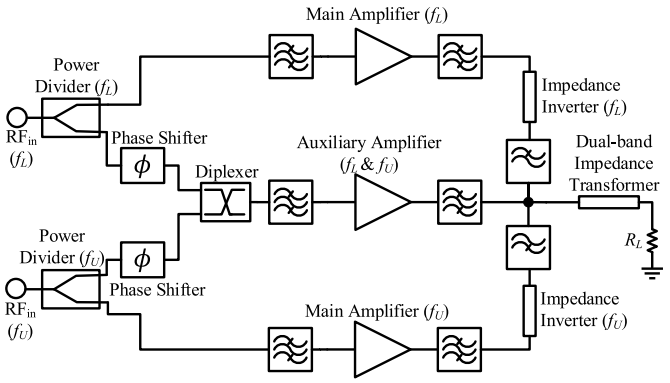

Fig. 1. Diagram of the proposed 3-Way DB-DPA.

efficiency and PAPR of these DB-DPAs were significantly improved. However, most of these DB-DPA papers focus on improving the drain efficiency of each band instead of the total average efficiency under concurrent operation.

By using new techniques in the concurrent DB-DPA such as eliminating the IM generated from the two signals [13], using a crest factor reduction (CFR) technique [18] and power tracking technique [19], the performance of concurrent DB-DPA's was successfully improved. Some of these techniques are used at the design stage of the PA, and some are performed at the linearization stage of the DB-DPA when using modulated signals. A 3-Way DB-DPA realized by adding another auxiliary PA was studied to extend the PAPR in SB operation [16]. It can be inferred that the DB-DPA's concurrent performance can be optimized but still remains fundamentally limited by its architecture.

In this article, a novel architecture of the DB-DPA (3-Way DB-DPA) is proposed. The architecture of the novel 3-Way DB-DPA is shown in Fig. 1. Like other 3-Way PAs such as the 3-Way DPA [16] and the load-modulated balance amplifiers (LMBAs) [20], it consists of three amplifiers (three ways). The first two amplifiers are used as main (carrier) amplifiers, which both operate in class F. The third amplifier is the auxiliary (peaking) amplifier, which is shared by the two-band signals and operates in class C. Each main amplifier handles signals individually at either the lower band centered at f_L or the upper band centered at f_U to avoid early clipping as will be later explained in detail. This results in both higher power gain and total output power in the concurrent mode. Thus, the addition of a second main amplifier increases the total concurrent output power while also improving the concurrent total efficiency compared to the 2-Way DB-DPA. The absence of IM products in the main PAs that normally arise in the 2-Way DPA in dual-band operation also greatly simplifies the design of their matching networks. However, the second-order IM products at the frequencies $f_U - f_L$ and $f_L + f_U$ need to be properly terminated at the output of the auxiliary amplifier to further improve the DB-DPA's performance. It will be verified in Section I that a short is an optimal termination [13]. The two impedance inverters of the main amplifiers of the DPA are integrated as a part of their output combiner. In the output combiner, a diplexer realized with low- and high-pass filters is used to distribute the lower band and upper band load—pull signals between the main amplifiers so that no IM products are created. At the output of the 3-Way DB-DPA, a dual-band impedance transformer is also integrated as a part of the output power combiner. At the input of the 3-Way DB-DPA, two Wilkinson power dividers (WPDs) with uneven power ratio are designed for each RF band to divide the input power between the main amplifiers and the auxiliary amplifier. At the gate of the main amplifiers, a matching network that includes a proper termination for the input second harmonic is designed for the lower band and upper band signals. In addition, two 90° phase shifters are used in the auxiliary branch after the WPDs as shown in Fig. 1 to compensate for the phase offset between the main and auxiliary amplifiers introduced by the inverters. After the phase shifters, a diplexer is implemented at the input of the auxiliary amplifier to combine both signals and prevent the lower band signal from going to the upper band main amplifier and vice versa. A dual-band matching network that includes the termination of the lower band and upper band second harmonic is implemented at the gate of the auxiliary transistor.

The rest of this article is organized as follows. An analysis of the power distribution and clipping in dual-band operation is reported in Section I. An investigation of the impact of the relative phase in two-tone excitations on the continuous-wave (CW) performance of the new 3-Way versus conventional 2-Way DB-DPA's architectures is also presented in that section. In addition, a study of the impact of IM products on the performance of dual-band class-F PAs is investigated in Section I, to demonstrate the advantage of using separate main PAs. Following these preliminary investigations, a general design theory for the 3-Way DB-DPA is presented in Section II to compare the new 3-Way DB-DPA with the traditional 2-Way DB-DPA. The design procedure and harmonic balance simulation results for the 3-Way DB-DPA using a realistic device model are presented in Section III. A statistical study of the efficiency at the current-source reference planes (CSRPs) is also reported in that section. Section IV gives the CW and modulated measurement results obtained for the fabricated 3-Way DB-DPA. In the conclusion, a summary of the results obtained is presented in Section V.

I. Analysis of Dual-Band Signals in PA

A. Effect of Clipping and Phase in Dual-Band Operation

In the proposed 3-Way DB-DPA, the main amplifiers handle each band separately, whereas the auxiliary amplifier is shared by the two lower and upper band signals. Therefore, these two CW signals will be beating at the auxiliary amplifier: the two CW signals add up constructively when they are in-phase and cancel when they are out-of-phase.

Accounting for the gate V_{GG} and drain V_{DD} dc bias voltages, the gate $v_{GS,a}(t)$ and drain $v_{DS,a}(t)$ voltage waveforms at the auxiliary transistor are expressed as follows:

$$\begin{aligned} v_{GS,a}(t) &= V_{GG} + |V_{GSa,L}|\cos(2\pi f_L t) \\ &\quad + |V_{GSa,U}|\cos(2\pi f_U t + \delta\phi) \\ v_{DS,a}(t) &= V_{DD} + |V_{a,L}|\cos(2\pi f_L t + \pi) \\ &\quad + |V_{a,U}|\cos(2\pi f_U t + \pi + \delta\phi) \end{aligned}$$

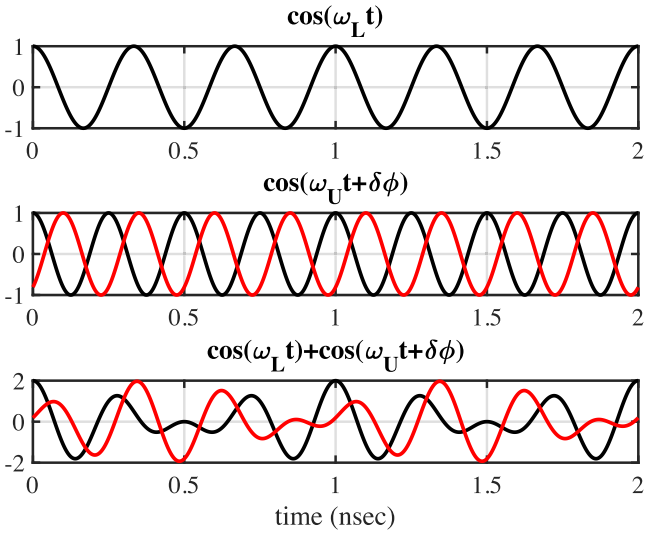

Fig. 2. CW signals for the lower band (top) and upper band with two different phase offsets (center) and combined waveforms (bottom).

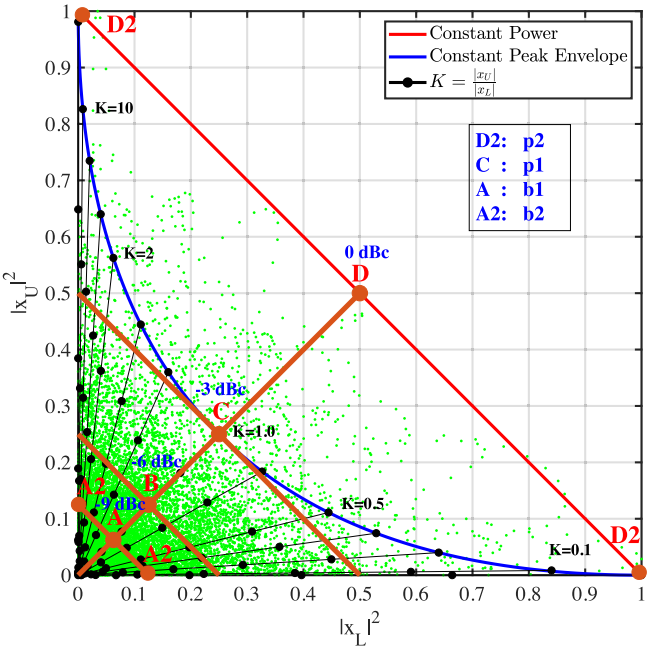

Fig. 3. Power distribution in dual-band PAs, associated modes of operation (A–D) and clipping boundary (blue line).

where the phase of the first band is set to zero and the phase of the second band is set to the phase offset $\delta\phi$ between the lower and upper band CW signals to simplify the notation.

The lower band and upper band CW signals are plotted in Fig. 2 for two different phase offsets $\delta\phi$ for the upper band signal. As the phase offset varies, the combined waveforms exhibit a similar constructive and destructive behavior in concurrent (C) operation.

The cosine subwaveforms will constructively add when in-phase to nearly the same maximum and minimum values, independently of the phase offset

$$v_{\mathrm{GS},a}^{\max}(\mathrm{C}) = V_{\mathrm{GG}} + (|V_{\mathrm{GSa},L}| + |V_{\mathrm{GSa},U}|)$$
$$v_{\mathrm{DS},a}^{\min}(\mathrm{C}) = V_{\mathrm{DD}} - (|V_{a,L}| + |V_{a,U}|).$$

The RF drives $V_{\mathrm{GSa},L/U}$, for which the maximum gate voltage is the threshold voltage: $v_{\mathrm{GS},a}^{\max}(\mathrm{C}) = V_T$, will determine the backoff condition at which the auxiliary transistor turns on in dual-band operation. Similarly, the RF drives, for which the minimum drain voltage reaches the transistor knee voltage: $v_{\mathrm{DS},a}^{\min}(\mathrm{C}) = V_{\mathrm{ON}}$, will determine the threshold at which the auxiliary transistor output voltage will start clipping in dual-band operation.

For convenience, let us introduce the normalized communication waveforms x_L and x_U defined either at the PA input or output

$$x_{L/U} = \overline{V_{a,L/U}} = \frac{V_{a,L/U}}{|V_{a,L/U}^{\max}|} \tag{1}$$

where $|V_{a,L/U}^{\max}|$ is the maximum RF drain voltage amplitude for the auxiliary transistor at saturation in the lower or upper band SB operation.

The 2-D normalized power distribution of two uncorrelated long-term evolution (LTE) signals before CFR at the PA input (or output after linearization) is shown in Fig. 3 versus the normalized signal powers $|x_L|^2$ and $|x_U|^2$ using green dots. The four diagonal lines crossing the points (D2-D-D2), C, B, and (A2-A-A2) are the constant-power contour lines corresponding to 0, −3, −6, and −9 dBc, respectively, using the peak power in SB operation as a reference.

To avoid having the auxiliary PA voltage clipping at peak power under concurrent operation, the two-band RF signals x_L and x_U need to verify at peak power

$$|x_L| + |x_U| \leq 1$$

so that the auxiliary loadline does not enter the triode region. The blue line in Fig. 3 corresponds to the clipping threshold $|x_L^{\mathrm{clip}}| + |x_U^{\mathrm{clip}}| = 1$. It is verified that the majority of the two-band LTE data are located below the clipping threshold.

The diagonal line from A to C corresponds to the concurrent-balanced (CB) mode. Note that the peak power $P_{\mathrm{out}}^{\mathrm{peak}}(\mathrm{CB})$ for the CB operation without clipping occurs at point C. The peak power $P_{\mathrm{out}}^{\mathrm{peak}}(\mathrm{CB})$ in the CB mode (point C) is exactly half the peak power $P_{\mathrm{out}}^{\mathrm{peak}}(\mathrm{SB})$ in the SB mode (points D2).

A variable K is introduced as the ratio of $|x_U|$ to $|x_L|$ of the two signal amplitudes. The $K = 1$ line thus corresponds to the CB mode.

The impact upon a DPA of the phase offset $\delta\phi$ between two CW signals x_L and x_U is now investigated. For this purpose, simulations using the new 3-Way DB-DPA are performed at the CSRP to observe the impact of the phase $\delta\phi$ on the concurrent efficiency. For each phase $\delta\phi$, the PA's efficiency is obtained for all of the 84 ($|x_L|$,$|x_U|$) points represented by black dots in Fig. 3. The total drain efficiency for the 84 points calculated for seven phase offsets $\delta\phi$ is shown in Fig. 4. As it can be seen, the phase offset between the two signals has a negligible impact on the 3-Way DB-DPA total drain efficiency. This insensitivity on the phase offset $\delta\phi$ will also be verified in CW concurrent measurements in Section IV.

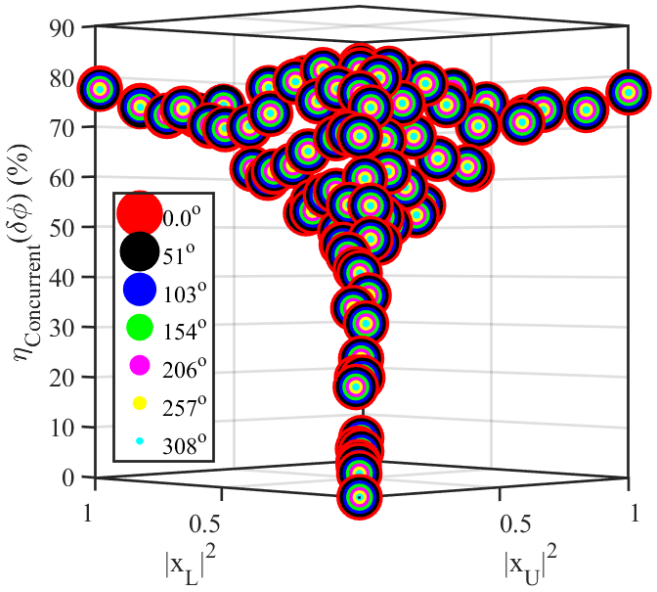

Fig. 4. 3-Way DB-DPA total drain efficiency at the CSRP while varying the phase offset between x_L and x_U.

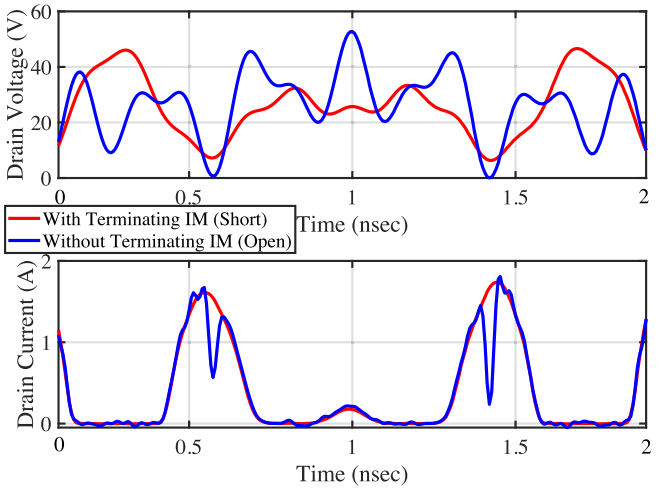

Fig. 5. Comparison of drain voltage (top) and current (bottom) waveforms with an open (blue) and a short (red) terminating the second-order IM products.

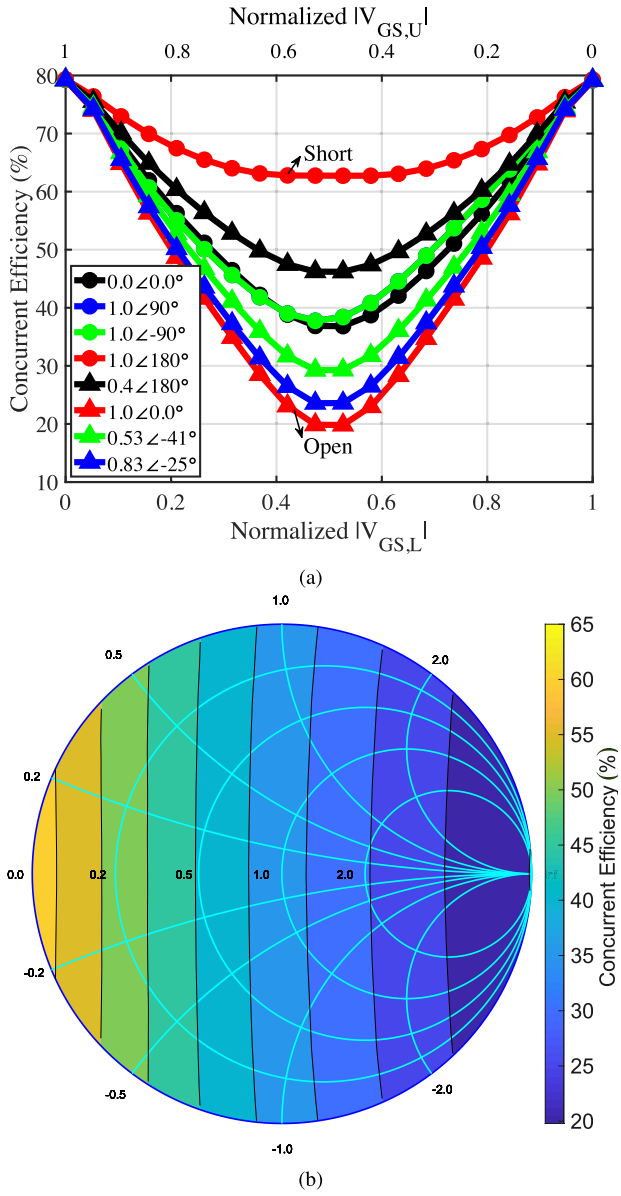

Fig. 6. Effects of the termination of the second-order IM products on a class-F PA: (a) efficiency plotted versus the normalized input voltage $|V_{GS,L/U}|$ for different values of $\Gamma_L(f_U - f_L) = \Gamma_L(f_L + f_U)$ and (b) contour plot of the efficiency in the $\Gamma_L(f_U - f_L) = \Gamma_L(f_L + f_U)$ plane.

It can be concluded that the 3-Way DB-DPA performance is essentially independent on the phase offset $\delta\phi$, which will simplify the theoretical analysis in Section II.

B. Dual-Band Class-F PA IM Effects

When two CW signals with different operating frequencies are amplified simultaneously, the interaction of the two CW signals via the nonlinearities of the transistors creates IM products at the terminals of the transistor that impact the dual-band PA's performance. These IM effects are investigated now at the CSRP in the case of a single dual-band class-F PA. Among all the various IM products, those of second-order are found to be the most important ones due to their large impact on the PA performance. The second-order IM nonlinearities generate terms with frequencies $f_U - f_L$ and $f_L + f_U$. A comparison of the voltage (top) and current (bottom) waveforms at the drain of transistor with open (blue plain line) and short (red plain line) load terminations for the second-order IM products is presented in Fig. 5. This figure shows that the current and voltage waveforms are smoother and less distorted when using a short at the drain for the second-order IM products.

In order to assess the impact of the impedance termination for the second-order IM products on the concurrent efficiency of the dual-band class-F PA, the PA's efficiency is calculated for load reflection coefficients $\Gamma_L(f_U - f_L)$ and $\Gamma_L(f_L + f_U)$ varying along the constant peak envelope (blue line in Fig. 3 corresponding here to $|\overline{V_{GS,mL}}| + |\overline{V_{GS,mU}}| = 1$). The resulting efficiencies are plotted in Fig. 6(a) versus the normalized gate drive $\overline{V_{GS,mU/L}}$ (K factor varying from 0 to 100) for eight different values of $\Gamma_L(f_U - f_L) = \Gamma_L(f_L + f_U)$.

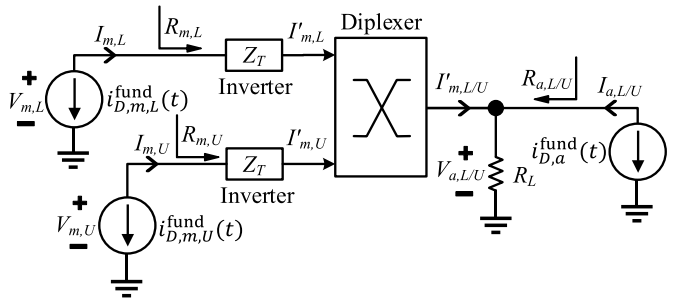

Fig. 7. Circuit of the novel DB-DPA at the drain CSRP for the fundamental frequencies.

The DB-DPA must operate for all the different concurrent operating modes. However, the CB mode ($K = 1$) is the most important mode as this is the mode that emphasizes the dual-band PA performance. In the CB mode at $K = 1$, a large variation in the concurrent efficiency from 20% to 65% can be observed in Fig. 6 as $\Gamma_L(f_U - f_L) = \Gamma_L(f_L + f_U)$ varies from open to short.

The selection of $\Gamma_L(f_U - f_L)$ and $\Gamma_L(f_L + f_U)$ is thus critical in the dual-band PA. It is verified in the contour plot in Fig. 6(b) based on 125 different loads that the maximum efficiency is obtained when using a short for the second-order IM products ($\Gamma_L(f_U - f_L) = \Gamma_L(f_L + f_U) = -1$) at the CSRP. Therefore, for optimal performance, the second-order IM products of both the main and auxiliary transistors will be properly terminated in the 2-Way DB-DPA used for comparison. In the 3-Way DB-DPA, the second-order IM products at the auxiliary amplifier will be similarly terminated. However, no IM load termination will be needed for the main amplifiers because each amplifier is isolated by diplexers to handle an SB.

II. Theory for the Proposed 3-Way DB-DPA

A. Three-Way DB-DPA Design Theory

In this section, the design equations of the new 3-Way DB-DPA will be derived at the CSRP of the transistors. The transistors are modeled by current sources representing the I–V characteristics at the CSRP. The diagram that represents the 3-Way DB-DPA is shown in Fig. 7.

In the novel 3-Way DB-DPA, two main amplifiers are used such that each main amplifier handles an SB. The fundamental drain voltages and currents of the two main transistors at the lower band and upper band are noted as $V_{m,L}$ and $V_{m,U}$ and $I_{m,L}$ and $I_{m,U}$, respectively. The fundamental drain voltages and currents of the single auxiliary transistor at the lower band and upper band are noted as $V_{a,L}$ and $V_{a,U}$ and $I_{a,L}$ and $I_{a,U}$, respectively. The fundamental drain currents in the time domain for the 3-Way DB-DPA are then given by

$$i_{D,m,L/U}^{\text{fund}}(t) = \text{Re}\{I_{m,L/U}e^{j\omega_{L/U}t}\}$$
$$i_{D,a}^{\text{fund}}(t) = \text{Re}\{I_{a,L}e^{j\omega_L t} + I_{a,U}e^{j\omega_U t}\}.$$

The 3-Way DB-DPA will behave as a normal Doherty PA when operating in the SB mode and as a modified Doherty PA in the concurrent operation. In CB operation, the auxiliary transistor will turn on earlier and the DB-DPA exhibits an early backoff occurring at the fundamental main gate voltage $V_{\text{GSm},b1}$ noted with the subscript $b1$. In SB operation, the DB-DPA exhibits a later backoff at the fundamental main gate voltage drive $V_{\text{GSm},b2} = 2 \times V_{\text{GSm},b1}$ noted with the subscript $b2$. Note that the output backoff (OBO) of the SB and CB modes corresponding to point A2 and A, respectively, in Fig. 3, occurs for the same total output power. Indeed, the backoff powers $P_{\text{out},L}^{\text{back}}(\text{SB})$ or $P_{\text{out},U}^{\text{back}}(\text{SB})$ in the SB mode are equal to total backoff power $P_{\text{out},L}^{\text{back}}(\text{CB}) + P_{\text{out},U}^{\text{back}}(\text{CB})$ in the CB mode. The associated backoff voltages and currents are noted: V_{mb1}, V_{mb2}, I_{mb1}, and I_{mb2} for the main transistors and V_{ab1}, V_{ab2}, I_{ab1}, an I_{ab2} for the auxiliary transistor.

Similarly, the 3-Way DB-DPA exhibits two different peak operations in the SB and CB modes. In CB operation, the DB-DPA saturates earlier, at the fundamental main gate voltage $V_{\text{GSm},p1}$. In SB operation, the DB-DPA saturates later on, at the fundamental main gate voltage $V_{\text{GSm},p2}$. The associated saturation voltages and currents are noted: V_{mp1}, V_{mp2}, I_{mp1}, and I_{mp2} for the main transistors and V_{ap1}, V_{ap2}, I_{ap1}, and I_{ap2} for the auxiliary transistor, respectively.

Note that in both CB and SB modes, the lower band and upper band voltages and currents have the same amplitudes at the CSRP.

For clarity, the variation of the main and auxiliary currents and voltages versus the input RF drive, which will be obtained from the final design theory presented in this section, is shown in Fig. 8(a) and (b) for both the SB and CB modes. The critical target under the prevalent CB mode of operation for high-efficiency operation is to have the peak auxiliary fundamental voltages that verify

$$|V_{\text{ap1},L}| + |V_{\text{ap1},U}| = 2|V_{\text{ap1}}| = |V_{\text{ap2}}| \tag{2}$$

so as to maximize the auxiliary PA's efficiency when it reaches the clipping threshold (point C in Fig. 3). Similarly, to maximize the drain PA's efficiencies in the CB mode of operation, we need ideally to have the main drain voltage approaching the SB mode value at the clipping threshold (point C)

$$|V_{\text{mp1,L}}| = |V_{\text{mp1,U}}| \simeq |V_{\text{mp2}}|. \tag{3}$$

From the auxiliary CB condition in (2): $|V_{\text{ap1}}| = |V_{\text{ap2}}|/2$, it follows that the main peak currents at point C verify $I_{\text{mp1}} = I_{\text{mp2}}/2$ in virtue of the property of the inverters. It also results that the total power $P_{\text{out}}^{\text{peak}}(\text{CB})$ at the load R_L at point C of the CB mode is half the power $P_{\text{out}}^{\text{peak}}(\text{SB})$ of the SB mode since we have

$$P_{\text{out}}^{\text{peak}}(\text{CB}) = \frac{1}{2R_L}|V_{\text{ap1},L}|^2 + \frac{1}{2R_L}|V_{\text{ap1},U}|^2$$
$$= \frac{1}{4R_L}|V_{\text{ap2},L/U}|^2 = \frac{1}{2}P_{\text{out}}^{\text{peak}}(\text{SB}).$$

Given that the active loads R_{mp1} and R_{ap1} seen by the main and auxiliary transistors at the CB model peak power are

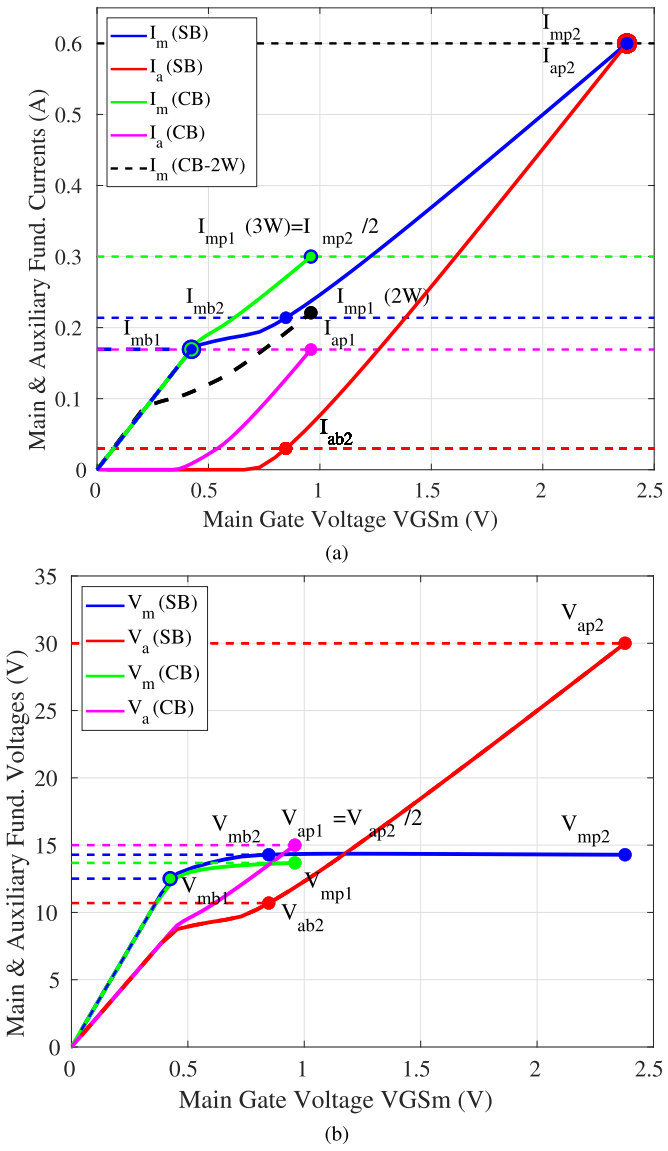

Fig. 8. Fundamental (a) currents and (b) voltages versus the main gate drives for the main and auxiliary amplifiers at the CSRP in both the SB and CB modes.

given by

$$R_{\rm mp1} = \frac{Z_T^2}{R_L\left(1+\frac{Z_T|I_{\rm ap1}|}{|V_{\rm mp1}|}\right)}$$
$$R_{\rm ap1} = R_L\left(1+\frac{|V_{\rm mp1}|}{Z_T|I_{\rm ap1}|}\right)$$

the auxiliary and main drain voltage equations (2) and (3) yield the solution

$$|I_{\rm ap1}| = \frac{|V_{\rm ap2}|}{2R_L} - \frac{|V_{\rm mp1}|}{Z_T}, \quad (4)$$
$$= |I_{\rm ap2}| - \frac{|V_{\rm ap2}|}{2R_L}, \text{ if } |V_{\rm mp1}| = |V_{\rm mp2}|. \quad (5)$$

Under such a condition, where the auxiliary and main drain voltages are maximized, a high-efficiency operation is achieved in the CB mode while delivering half the peak SB power as targeted at the clipping point C in Fig. 3.

The design of the DB-DPA makes use of the DPA theory developed in [6] where six design parameters are used. These six parameters include $|I_{\rm ap2}|$ and $|V_{\rm ap2}|$ introduced above and n, $\gamma_{\rm vp}$, $K_{\rm vm2}$, and $K_{\rm ia2}$ introduced next.

Note that the peak fundamental current $|I_{\rm ap2}|$ and voltage $|V_{\rm ap2}|$ of the auxiliary device are usually selected as the maximum drain current and voltage of the transistor, respectively.

The factor n is the asymmetry power ratio between the auxiliary and main PAs for a DPA in SB operation as defined in [21]

$$n = \frac{P_{\rm ap2}}{P_{\rm mp2}} = \frac{|V_{\rm ap2}||I_{\rm ap2}|}{|V_{\rm mp2}||I_{\rm mp2}|} \quad (6)$$

where $P_{\rm ap2}$ and $P_{\rm mp2}$ refer to the fundamental peak powers delivered by the auxiliary and main PAs in SB operation, respectively.

The factor $\gamma_{\rm vp} = |V_{\rm mp2}|/|V_{\rm ap2}|$ is the main-to-auxiliary peak voltage ratio in SB operation. The factor $K_{\rm vm2} = |V_{\rm mp2}|/|V_{\rm mb2}|$ is the peak-to-backoff main voltage ratio in SB operation. The factor $K_{\rm ia2} = |I_{\rm ap2}|/|I_{\rm ab2}|$ is the peak-to-backoff auxiliary voltage ratio in SB operation.

The six above parameters are sufficient to design a normal DPA and are thus applicable to the DB-DPA for SB operation from backoff to peak power. For concurrent operation, additional design considerations are needed to handle the CB backoff while retaining compatibility with the SB operation. To make the SB and CB modes compatible, we will see that the main loadline in the SB mode needs to enter the triode region to both clip the main drain voltage and reduce the effective main transistor transconductance between the CB and SB backoffs. This early saturation in SB band operation is needed so that the main transistors can reach the drain current $I_{\rm mb1}$ in the CB mode at the early CB backoff where the auxiliary transistor turns on.

To present the novel design procedure for the 3-Way DB-DPA, a quasi-analytic solution is presented for the case of a piecewise linear I–V model with a threshold voltage V_T, knee voltage $V_{\rm ON}$, and constant transconductance g_m, as shown in Fig. 9.

The asymmetry power ratio verifies [22]: $n = 1/(\gamma_{\rm vp}\gamma_{ip})$. In this example, we select $\gamma_{\rm vp} = 1/n$ so that $\gamma_{ip} = |I_{\rm mp2}|/|I_{\rm ap2}| = 1$. We thus have $|V_{\rm mp2}| = \gamma_{\rm vp}|V_{\rm ap2}|$ and $|I_{\rm mp2}| = |I_{\rm ap2}|$.

The peak-to-backoff auxiliary voltage ratio in SB operation $K_{\rm im2}$ is given by

$$K_{\rm im2} = \frac{|I_{\rm mp2}|}{|I_{\rm mb2}|} = \frac{K_{\rm vm2}(n+1)}{1+n\frac{K_{\rm vm2}}{K_{\rm ia2}}}.$$

The SB backoff main current is then given by $|I_{\rm mb2}| = |I_{\rm mp2}|/K_{\rm vm2}$. The main current ratio $K_{\rm im2}$ determines also the SB OBO power OBO $= K_{\rm im2}^2$ [6]. In this example, we select $n = 2.1$, yielding an OBO of 9 dB in the SB mode. Using the auxiliary current ratio $K_{\rm ia2}$, we obtain the SB auxiliary backoff current $|I_{\rm ab2}| = |I_{\rm ap2}|/K_{\rm ia2}$.

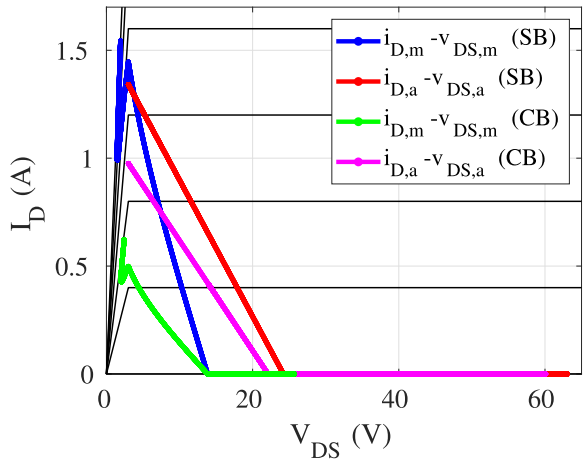

Fig. 9. Piecewise linear I–V characteristics and loadlines of the main and auxiliary transistors at peak power in the SB and CB modes.

The characteristic impedance Z_T of the $\lambda/4$ transformer and the common load R_L is obtained from [6]

$$Z_T = \frac{|V_{\rm mb2}||I_{\rm mp2}| - |V_{\rm mp2}||I_{\rm mb2}|}{|I_{\rm mb2}||I_{\rm ap2}| - |I_{\rm mp2}||I_{\rm ab2}|}$$

$$R_L = \frac{(|V_{\rm mb2}||I_{\rm mp2}| - |V_{\rm mp2}||I_{\rm mb2}|)^2}{(|I_{\rm mb2}||I_{\rm ap2}| - |I_{\rm mp2}||I_{\rm ab2}|)(|V_{\rm mb2}||I_{\rm ap2}| - |V_{\rm mp2}||I_{\rm ab2}|)}.$$

These equations can alternatively be expressed in the terms of the DPA design parameters as

$$Z_T = nR_{\rm opt}\gamma_{\rm vp} \text{ and } R_L = \frac{n}{n+1}R_{\rm opt} \text{ with } R_{\rm opt} = \frac{|V_{\rm ap2}|}{|I_{\rm ap2}|}.$$

For the example selected in Table I, we obtain $Z_T = 50\ \Omega$ and $R_L = 33.87\ \Omega$.

To complete the design, we now need to determine the main fundamental drain current $I_{\rm mb1}$ and voltage $V_{\rm mb1}$, as well as the gate and drain dc biases for both the main and auxiliary PAs and the coupler coefficient C_p relating the main and auxiliary RF gate drives.

Let us first consider the two main amplifiers. They are assumed to operate in an ideal three-harmonic class-F mode, with a drain voltage $v_{{\rm DS},mL/U}$ for the band L/U given by

$$v_{{\rm DS},m,L/U}(t) = V_{{\rm DD},m} + {\rm Re}\left\{|V_m|e^{j\omega_{L/U}t} - \frac{|V_m|}{3}e^{j3\omega_{L/U}t}\right\}$$

with $V_{{\rm DD},m}$ the main dc drain bias to be determined. As was verified in Section I, the phases of the two bands do not affect the device performance and are set to zero. The dc gate bias $V_{{\rm GG},m}$ for the main PAs is simply set to the threshold voltage V_T of the transistor so that we have

$$v_{{\rm GS},m,L/U}(t) = V_{{\rm GG},m} + {\rm Re}\left\{V_{{\rm GS},m}e^{j\omega_{L/U}t}\right\}$$

with $V_{{\rm GS},m}$ the main fundamental gate voltage. The main fundamental drain current can then be written as

$$I_m = \begin{cases} \dfrac{1}{2}g_m V_{{\rm GS},m} \text{ for } V_m \le V_{\rm DS}^{\rm clip} \\ \dfrac{1}{2}g_m^{\rm clip}[V_{\rm DS}, V_{{\rm DD},m}]V_{{\rm GS},m} \text{ for } V_{\rm DS}^{\rm clip} < V_m \le V_{\rm DS}^{\rm max} \end{cases}$$

TABLE I

INPUT AND OUTPUT DESIGN PARAMETERS

Input Design Parameters					
$\lvert V_{ap2}\rvert$ (V)	$\lvert I_{ap2}\rvert$ (A)	n	γ_{vp}	K_{vm2}	K_{ia2}
30	0.6	2.1	0.4762	1	20
Output Design Parameters					
$\lvert V_{mp1}\rvert$ (V)	$\lvert I_{mp1}\rvert$ (A)	$\lvert V_{mp2}\rvert$ (V)	$\lvert I_{mp2}\rvert$ (A)	$\lvert V_{ap1}\rvert$ (V)	$\lvert I_{ap1}\rvert$ (A)
13.684	0.3	14.286	0.6	15	0.1692
$\lvert V_{mb1}\rvert$ (V)	$\lvert I_{mb1}\rvert$ (A)	$\lvert V_{mb2}\rvert$ (V)	$\lvert I_{mb2}\rvert$ (A)	$\lvert V_{ab2}\rvert$ (V)	$\lvert I_{ab2}\rvert$ (A)
12.510	0.1695	14.286	0.2139	10.695	0.030
$V_{GG,m}$ (V)	$V_{DD,m}$ (V)	$V_{GG,a}$ (V)	$V_{DD,a}$ (V)	V_{on} (V)	g_m (S)
-3	13.834	-3.694	33	3	0.8
$V_{GS,mb1}$ (V)	$V_{GS,mb2}$ (V)	$V_{GS,mp1}$ (V)	$V_{GS,mp2}$ (V)	V_T (V)	C_p
0.4237	0.8475	0.9598	2.378	-3	0.9971

where $g_m^{\rm clip}[V_m, V_{{\rm DD},m}]$ is a nonlinear function of V_m and $V_{{\rm DD},m}$ which can easily be tabulated for the $V_{\rm ON}$ and g_m parameters used. The clipped transconductance $g_m^{\rm clip}[V_m, V_{{\rm DD},m}]$ varies from g_m at the clipping threshold $V_{\rm DS}^{\rm clip} = (V_{\rm DD} - V_{\rm ON})/\nu_{\rm DS}^{\rm max}$ to about $0.2323 \times g_m$ (for $V_{{\rm DD},m} = 30$ V) at the maximum fundamental drain voltage $V_{\rm DS}^{\rm max} = V_{\rm DD}/\nu_{\rm DS}^{\rm max}$ with $\nu_{\rm DS}^{\rm max} = \max\{\cos(\omega_{L/U}t) - \cos(3\omega_{L/U}t)/6\}$ approximately equal to 0.8660.

At the lower CB backoff, the main transistors are still operating in the linear regime. The fundamental drain current $I_{\rm mb1}$ at the low CB backoff is then simply related to the fundamental main drain voltage by: $V_{{\rm GS},bm1} = 2\ I_{\rm mb1}/g_m$. with the drain current related to the main fundamental drain voltage $V_{\rm mb1}$ to be determined by: $I_{\rm mb1} = R_L V_{\rm mb1}/Z_T^2$. Note that at the CB and SB thresholds, the auxiliary gate drive verifies $V_{{\rm GG},a} + 2|V_{{\rm GS},ab1}| = V_T$ and $V_{{\rm GG},a} + |V_{{\rm GS},ab2}| = V_T$, respectively. It results that we must have $|V_{{\rm GS},ab2}| = 2|V_{{\rm GS},ab1}|$ and, thus, $|V_{{\rm GS,mb2}}| = 2|V_{{\rm GS,mb1}}|$ since the auxiliary and main fundamental gate voltages are linearly related by the coupler. At the lower CB threshold, the main transistors are on the verge of clipping and verify the condition

$$V_{{\rm DD},m} - \nu_{\rm DS}^{\rm max}|V_{\rm mb1}| = V_{\rm ON}.$$

The final selection for $|V_{\rm mb1}|$ is then determined by a self-consistent solution of the main drain current at the higher SB threshold

$$I_{\rm mb2} = \frac{1}{2}g_m^{\rm clip}[V_{\rm mb2}, V_{{\rm DD},m}]V_{\rm GS,mb2}$$
$$= 2g_m^{\rm clip}[V_{\rm mb2}, \nu_{\rm DS}^{\rm max}V_{\rm mb1} + V_{\rm ON}]\frac{R_L}{g_m Z_T^2}V_{\rm mb1}$$

which is solved by interpolation using the known main $V_{\rm mb2}$ and $I_{\rm mb2}$ SB threshold voltage and current, respectively. The result obtained for $|V_{\rm mb1}|$ is shown in Table I for the example considered.

Next, we can similarly calculate the required main drain drive $V_{\rm GS,mp2}$ to obtain the targeted main peak drain current $I_{\rm mp2}$

$$I_{\rm mp2} = \frac{1}{2}g_m^{\rm clip}[V_{\rm mp2}, V_{{\rm DD},m}]V_{\rm GS,mp2}$$

using $|V_{\rm mp2}| = K_{\rm vm2}|V_{\rm mb2}|$.

Let us now turn toward the design of the auxiliary PA. The auxiliary PA is operating in class C and assumed to remain in the linear region of the I–V characteristic. Note that both the

lower $V_{a,L}$ and upper $V_{a,U}$ band voltages are applied to the drain of the auxiliary transistor such that the total auxiliary drain voltage $v_{\mathrm{DS},a}$ is given by

$$v_{\mathrm{DS},a}(t) = V_{\mathrm{DD},a} + \mathrm{Re}\{V_{a,L}e^{j\omega_L t} + V_{a,U}e^{j\omega_U t}\}$$

with $V_{\mathrm{DD},a}$ the auxiliary dc drain bias to be determined. As discussed in Section I, the phases of the two-band signals do not significantly affect the peak device performance and are set to zero. In the CB mode, the RF voltages of both bands are equal in magnitude: $|V_a| = |V_{a,L}| = |V_{a,U}|$. At maximum power in both the SB and CB modes, the peak voltages $|V_{\mathrm{ap2}}| = |V_{\mathrm{ap1},L}| + |V_{\mathrm{ap1},U}|$ are such that the loadlines reach the edge of the triode region without entering it. It results that the auxiliary dc drain bias must be selected according to the following equation:

$$V_{\mathrm{DD},a} = |V_{\mathrm{ap2}}| + V_{\mathrm{ON}}.$$

The auxiliary transistor is excited at the gate by the two-band signal

$$v_{\mathrm{GS},a}(t) = V_{\mathrm{GG},a} + \mathrm{Re}\{V_{\mathrm{GSa},L}e^{j\omega_L t} + V_{\mathrm{GSa},U}e^{j\omega_U t}\}$$

where $V_{\mathrm{GG},a}$ is the dc gate bias of the auxiliary PA and $V_{\mathrm{GSa},L/U}$ is the auxiliary fundamental gate voltages. In the CB mode, the two-band input RF signals verify $|V_{\mathrm{GSa}}| = |V_{\mathrm{GSa},L}| = |V_{\mathrm{GSa},U}|$. Note that these auxiliary fundamental gate voltages $V_{\mathrm{GSa},L/U}$ for the lower and upper bands are also linearly related to the main fundamental gate voltages $V_{\mathrm{GSm},L/U}$ using the coupling coefficient C_p

$$|V_{\mathrm{GS},a}| = C_p|V_{\mathrm{GS},m}|.$$

In the SB mode, the equation that defines the fundamental drain current for the auxiliary amplifier operating in class C is given by [23]

$$I_a = g_m W[\theta(V_{\mathrm{GG},a}, |V_{\mathrm{GS},a}|)] \times (|V_{\mathrm{GS},a}| + V_{\mathrm{GG},a} - V_T) \quad (7)$$

where $W[\theta]$ the conduction-angle weighting factor defined as

$$W[\theta] = \frac{1}{2\pi}\left(\frac{\theta - \sin\theta}{1 - \cos\frac{\theta}{2}}\right) \quad (8)$$

where θ is the conduction angle

$$\theta(V_{\mathrm{GG},a}, |V_{\mathrm{GS},a}|) = 2 \times \cos^{-1}\left(\frac{V_T - V_{\mathrm{GG},a}}{|V_{\mathrm{GS},a}|}\right). \quad (9)$$

The last two design parameters to determine are the auxiliary dc gate bias $V_{\mathrm{GG},a}$ and the coupling coefficient C_p. They are obtained by simultaneously solving the two transcendental equations associated with the auxiliary drain currents at peak and backoff in the SB mode

$$I_{\mathrm{ap2}} = g_m W[\theta(V_{\mathrm{GG},a}, |V_{\mathrm{GS},ap2}|)](|V_{\mathrm{GS},ap2}| + V_{\mathrm{GG},a} - V_T)$$
$$I_{\mathrm{ab2}} = g_m W[\theta(V_{\mathrm{GG},a}, |V_{\mathrm{GS},ab2}|)](|V_{\mathrm{GS},ab2}| + V_{\mathrm{GG},a} - V_T).$$

These monotonous equations are easily numerically solved by interpolation when sweeping the unknown variables $V_{\mathrm{GG},a}$ and C_p. The resulting values for the example considered are shown in Table I.

Having designed the 3-Way DB-DPA for the assumed piecewise linear I–V, we can then sweep the input gate voltage $V_{\mathrm{GS},m}$ and obtain the main and auxiliary fundamental currents and voltages versus the input RF drive, as shown in Fig. 8(a) and (b). Of particular interest is the peak auxiliary current I_{ap1} achieved in the CB mode. As shown in Table I, the magnitude of I_{ap1} from (4) is 0.169 A, whereas the estimate obtained from (5) is 0.1571 A when assuming $|V_{\mathrm{mp1}}| = |V_{\mathrm{mp2}}|$. The lower $|V_{\mathrm{mp1}}|$ value that approaches $|V_{\mathrm{mb1}}|$ provides for a larger transconductance g_m^{clip} and voltage gain. A more linear output voltage gain in the CB mode can be further achieved by selecting K_{vm2} smaller than one.

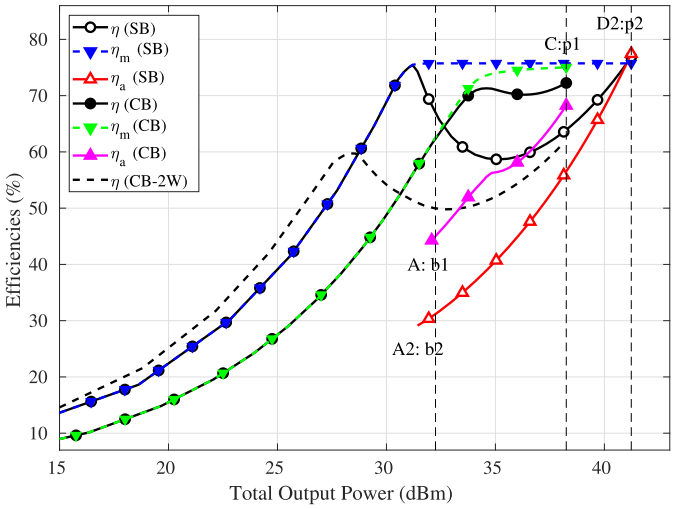

Fig. 10. Total, main, and auxiliary efficiencies for the SB and CB modes for the 3-Way DB-DPA and the total efficiency for the 2-Way DB-DPA (2W).

For the sake of comparison, the 3-Way DB-DPA designed can be used as a 2-Way DB-DPA by driving one of the main PAs with a dual-band signal. The auxiliary operation in the linear region is unaffected. However, the main current I_m(CB-2W) shown in Fig. 8(a) using black dashed line is seen to clip early at 0.25-V gate voltage and reach a lower I_{mp1}(2W) peak drain current in the CB mode.

The resulting efficiency versus total $(U + L)$ output power is shown in Fig. 10. The 3-Way DB-DPA sustains a high efficiency in the CB mode in a backoff range up to 6 dB below the peak power $P_{\mathrm{out}}^{\mathrm{peak}}$(CB) of the CB mode. We will see in Section III that this is the range of power in the CB mode with the highest probability when considering the joint probability distribution function (PDF) of the dual-band orthogonal frequency-division multiplexing (OFDM) signals considered. The individual contributions of the main and auxiliary PAs to the efficiency are separately itemized using

$$\eta = \frac{P_{\mathrm{out}}}{P_{\mathrm{dc}}} = \frac{P_{\mathrm{mL}} + P_{\mathrm{mU}} + P_{\mathrm{aL}} + P_{\mathrm{aU}}}{P_{\mathrm{dc,mL}} + P_{\mathrm{dc,mU}} + P_{\mathrm{dc},a}}$$
$$\eta_m = \frac{P_{\mathrm{out},m}}{P_{\mathrm{dc}}} = \frac{P_{\mathrm{mL}} + P_{\mathrm{mU}}}{P_{\mathrm{dc,mL}} + P_{\mathrm{dc,mU}}}$$
$$\eta_a = \frac{P_{\mathrm{out},a}}{P_{\mathrm{dc}}} = \frac{P_{\mathrm{aL}} + P_{\mathrm{aU}}}{P_{\mathrm{dc},a}}.$$

It is observed that at peak power, the main amplifiers jointly contribute a higher fraction of the output RF power than the auxiliary PA when operating in the CB mode unlike the SB mode where the auxiliary PA dominates.

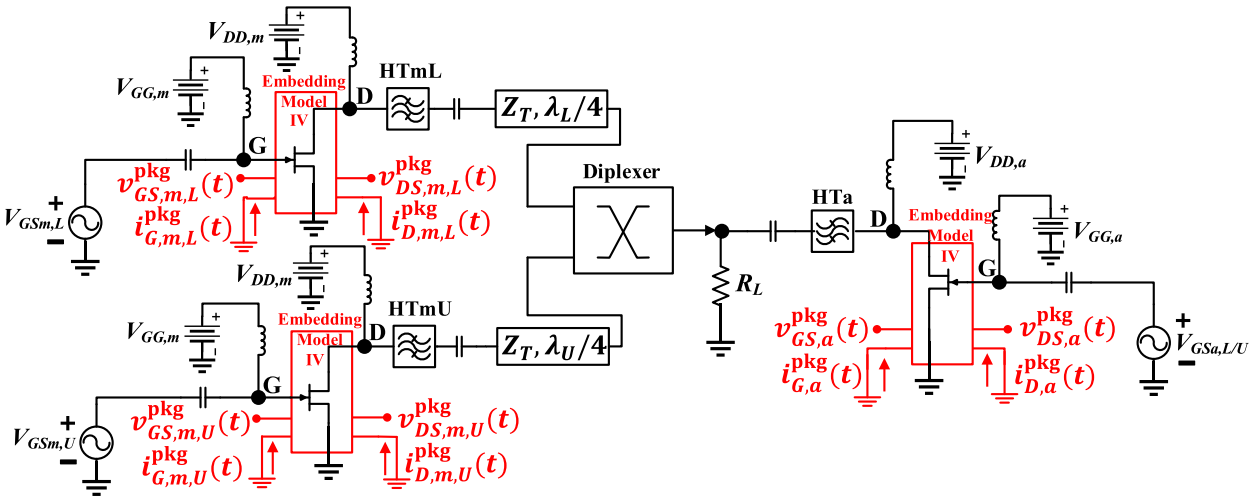

Fig. 11. Schematic of the 3-Way DB-DPA at the CSRP using the nonlinear embedding model.

TABLE II
INPUT AND OUTPUT DESIGN PARAMETERS AT THE CSRP FOR THE 3-WAY DB-DPA

Input Design Parameters					
n	γ_{vp}	K_{vm2}	K_{ia2}	I_{ap2}	V_{ap2}
1.76	0.58	1.09	258.4	0.6286 A	30.98 V
Output Design Parameters					
R_L	Z_T	$V_{GS,mp2}$	I_{mp2}	C_p	OBO
31 Ω	50 Ω	3.097 V	0.6197 A	1.15	9.0 dB

III. NEW 3-WAY DB-DPA DESIGN PROCEDURE AND SIMULATION RESULTS

A. 3-Way DB-DPA at the CSRP

The 3-Way DB-DPA of Fig. 1 was first implemented at the CSRP of the Cree CGH40010F gallium nitride (GaN) HEMT using the embedding Angelov model [23], as shown in Fig. 11. The embedding model provides a realistic I–V characteristic at the CSRP while at the same time projecting the CSRP waveforms to the package reference planes (PRPs) to facilitate the subsequent design of the PA circuit at the PRP. The red labeled voltages and currents in Fig. 11 represent the projected data at the PRP of the transistor.

The two main transistors on the left of Fig. 11 are operating in class F, with a gate bias voltage $V_{\mathrm{GG},m}$ of −2.9 V and drain bias voltage $V_{\mathrm{DD},m}$ of 16 V. The auxiliary transistor is operating in class C with a gate bias $V_{\mathrm{GG},a}$ of −4.2 V and drain bias $V_{\mathrm{DD},a}$ of 32 V.

The input design parameters and output circuit parameters of the 3-Way DB-DPA are shown in Table II. The input design parameters were tuned to obtain an optimal concurrent performance for the 3-Way DB-DPA at the CSRP when using the I–V of the Cree CGH40010F device. The design of the PA at the CSRP using the I–V of the transistor excludes the device parasitics and nonlinear charges, and thus, all the output harmonics were terminated by ideal shorts for the even harmonics and opens for the odd harmonics (circuits HTmL and HTmU in Fig. 11). The harmonic termination network at the drain for each of the main transistors is followed by an impedance inverter for its respective band. A diplexer is used to combine the two main amplifier outputs while preventing the signal of the lower band main amplifier from going to the upper band main amplifier and vice versa so that no IM will be created.

For the dual-band auxiliary amplifier, all the harmonics and the second-order IM products are shorted (circuit HTa in Fig. 11) at the intrinsic drain reference plane. Finally, the currents from the main and auxiliary amplifiers combine at the load R_L.

B. Simulation Setup and Results at the CSRP

The circuit in Fig. 11 is implemented in a harmonic balance circuit simulator to simulate and verify the circuit operation and performance of the 3-Way DB-DPA in the frequency domain at the CSRP. The input RF sources at f_L and f_U are swept from 0 to 2.7 V when the 3-Way DB-DPA is operating nonconcurrently. For the CB mode, the two input sources were swept simultaneously from 0 to 1.15 V.

SB harmonic balance simulation results at the CSRP for the 3-Way DB-DPA are shown in Fig. 12. The intrinsic drain efficiency and the projected drain efficiency at the package for each band are shown in Fig. 12. At the CSRP, the drain efficiencies for the lower band and upper band are the same because the model at the CSRP is frequency independent. The backoff drain efficiency is 75%, whereas the peak efficiency is 83% with 9.0-dB OBO. The projected drain efficiencies at the PRP for the lower and upper bands are slightly different due to the device parasitics, and their values degrade approximately by 3% from the intrinsic behavior. The SB projected power gains at the PRP for both bands are shown in Fig. 12. Their values vary between 18 and 24 dB. There is a drop in power gain above 33-dBm output power; this is due to the saturation of the two main amplifiers, while the load—pulling from the auxiliary is initiated. This saturation can be reduced to yield an increased gain by reducing K_{vm2} below one.

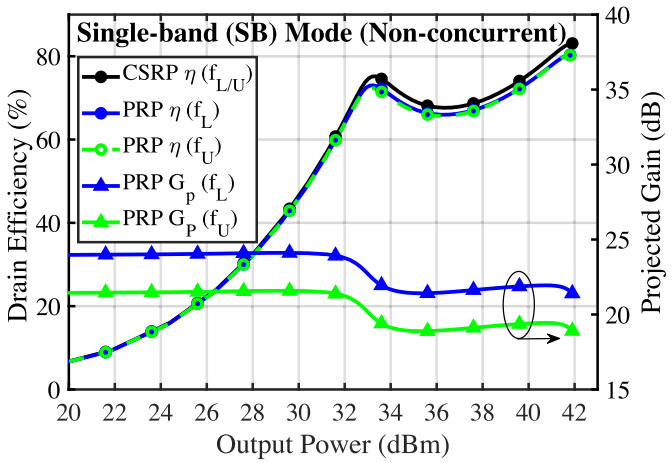

Fig. 12. Drain efficiencies and power gains at the CSRP and PRP obtained at f_L and f_U for the SB mode of operation using the embedding model.

All these simulation results are based on the ideal design of the 3-Way DB-DPA using the I–V characteristics of the Cree CGH40010F transistor provided by the embedding model.

The intrinsic and projected load impedances in the SB mode, seen by the upper band and lower band main transistors looking toward the load, are shown in Fig. 13(a). The intrinsic fundamental load impedances for the lower and upper bands that are represented by a black line with circles and a red line with triangles, respectively, are located along the real axis and give exactly the same impedance at the CSRP. As expected from a DPA, the fundamental load impedance changes from a large impedance at backoff to a small impedance at peak power due to the load modulation. The projected fundamental load impedances at the PRP for the lower and upper bands f_L and f_U are represented by a black line with triangles and a red line with circles, respectively.

The intrinsic second-harmonic load impedance of the main amplifiers (class F) are indicated by green circles and blue triangles on the far left of the real axis (short), while the intrinsic third-harmonic load impedance at both frequencies are indicated by pink circles and light blue triangles on the far right of the real axis (open) in Fig. 13(a). The projected second- and third-harmonic loads at the PRP for the main amplifiers are also shown in Fig. 13(a).

The intrinsic and projected load impedance seen by the dual-band auxiliary transistor looking toward the load are shown in Fig. 13(b). The intrinsic fundamental load impedance for both bands at the auxiliary transistor, which is represented by the black line with circles and red line with triangles, is located along the real axis and yields exactly the same impedances at the CSRP. They provide a very high impedance (open) when the auxiliary transistor is OFF. The projected fundamental load impedances at the PRP seen by the auxiliary amplifier in SB mode are shown in Fig. 13(b). For the auxiliary amplifier (class C), the intrinsic second and third harmonics for both bands are shorted as shown on the far left of the real axis. The projected second and third harmonics at the PRP are shown as well.

We next consider the case where the 3-Way DB-DPA is operated in CB mode. The intrinsic and projected package

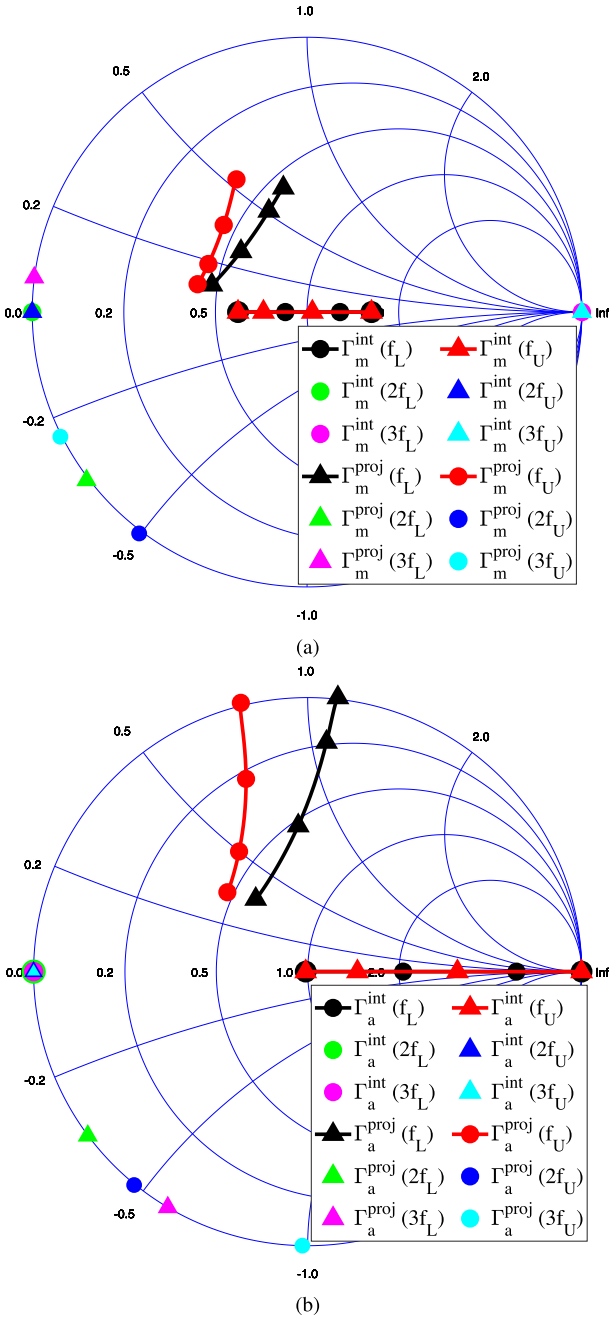

Fig. 13. Results in the SB mode for the load impedances seen by (a) main and (b) auxiliary transistors at the CSRP for the f_L and f_U frequencies, as the output power varies from backoff (A2) to peak power (D2).

drain efficiencies in CB mode are shown in Fig. 14. At peak power, the efficiency at the CSRP (black line) reaches 80%, whereas the efficiency at the PRP is projected to reach 77%. The total output power, where the 3-Way DB-DPA starts saturating (point C:p1 in Fig. 14) and the efficiency reaches its peak, is around 39 dBm or half the saturated output power in the SB mode (point D2:p2 in Fig. 3). This maximum-efficiency CB output power is associated with point C:p1 in Fig. 3, where the dual-band envelope starts clipping at the load. The OBO power in CB mode (point A:b1 in Figs. 3 and 14) is itself at 33-dBm total output power and this corresponds to 6 dB of backoff relative to point C instead of 9 dB relative to point

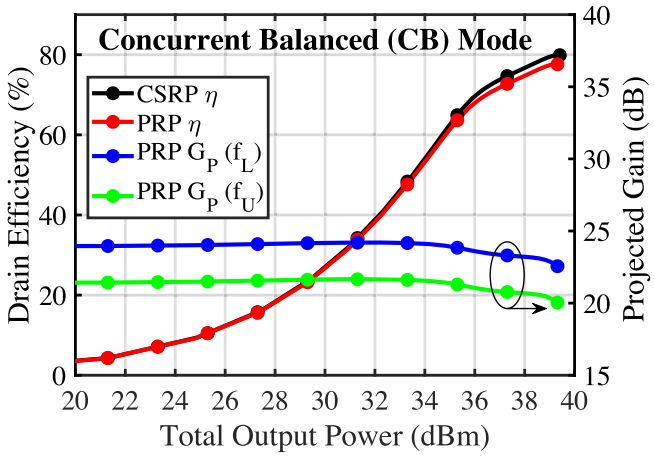

Fig. 14. CB operation mode in terms of drain efficiency and power gain for f_L and f_U at both the CSRP and PRP obtained from the nonlinear embedding model.

TABLE III
STATISTICAL AVERAGE PERFORMANCE AT THE CSRP OF THE 3- AND 2-WAY DB-DPAS

Average	2-Way DB-DPA	3-Way DB-DPA
$<\eta>$ (%)	46.1	61.2
$<P_{out}>$ (dBm)	30.2	34.3
$<P_{DC}>$ (dBm)	33.6	36.4
$<P_{out,L}>$ (dBm)	26.7	31.0
$<P_{out,U}>$ (dBm)	27.7	31.5

D2 in SB mode. The concurrent efficiency at the PRP for the OBO is around 48%, as shown in Fig. 14. The CB mode projected power gains at f_L and f_U are shown as well, in this figure. Compared to the SB mode, one can notice a much smaller decrease in power gain in CB above 33 dBm of total output power. This is due to the lighter saturation of the two main amplifiers in the CB mode when the auxiliary amplifier turns on.

The intrinsic and projected load impedances seen by the two mains and auxiliary amplifiers at both bands are shown in Fig. 15(a) and (b), respectively. The concurrent intrinsic fundamental load impedances seen by the main and auxiliary amplifiers start at the same high impedances at backoff as in the SB mode, but their peak impedances (at C:p1) do not reach the same low values of the SB mode (at D2:p2) due to the saturation of the auxiliary PA when the peak voltage envelope verifies $|V_{\text{ap1},U}| + |V_{\text{ap1},L}| = 2|V_{\text{ap1}}| = |V_{\text{ap2},U/L}|$. Fig. 15(b) also shows for the auxiliary amplifier how the shorted second-order IM products at the CSRP are projected to the PRP by the embedding model. As previously mentioned, these IM product terminations are critical for an optimal performance of the auxiliary PA, which is shared by the two bands.

C. Conventional 2-Way DB-DPA Versus the New 3-Way DB-DPA at CSRP

A comparison of the average performance of the 3- and 2-Way DB-DPAs at the CSRP is performed now using

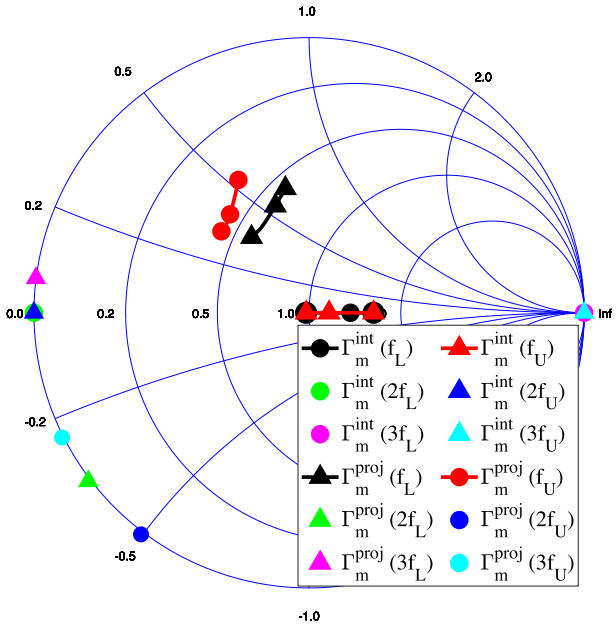

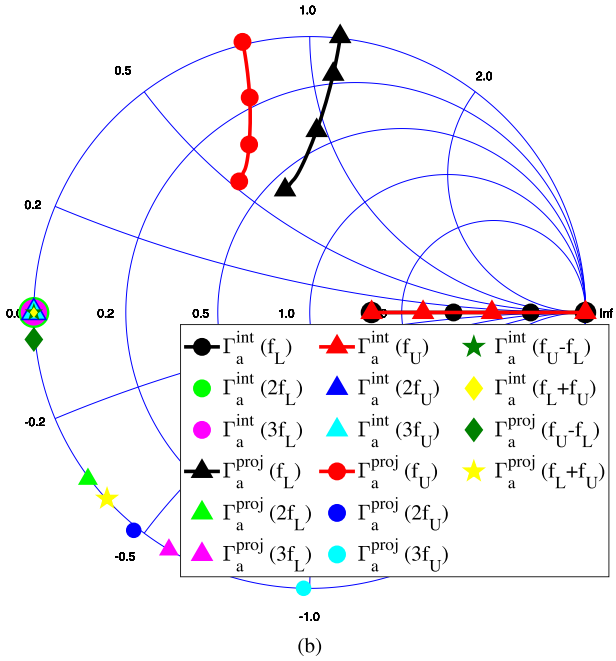

Fig. 15. Results in the CB mode for the load impedances seen by (a) main and (b) auxiliary transistors at the CSRP for the f_L and f_U frequencies, as the output power varies from backoff (A) to peak power (C).

a statistical analysis. Both DB-DPAs are operated with the same biasing so that they achieve the same SB performance. First, the concurrent CW performance of the two PAs is evaluated for 500 data points in the $(|x_L|^2, |x_U|^2)$ space. The resulting total drain efficiencies are plotted in the $(|x_L|^2, |x_U|^2)$ space using both 3-D and contour plots in Fig. 16(a) and (c) for the 2-Way DB-DPA and Fig. 16(b) and (d) for the 3-Way DB-DPA. Next, the average efficiencies are calculated, assuming that the PAs are excited by two uncorrelated signals with LTE PDF exhibiting each a PAPR of 6.25 and 6.35 dB. A summary of the results is shown in Table III. Using this statistical analysis at the CSRP, we can compare the expected

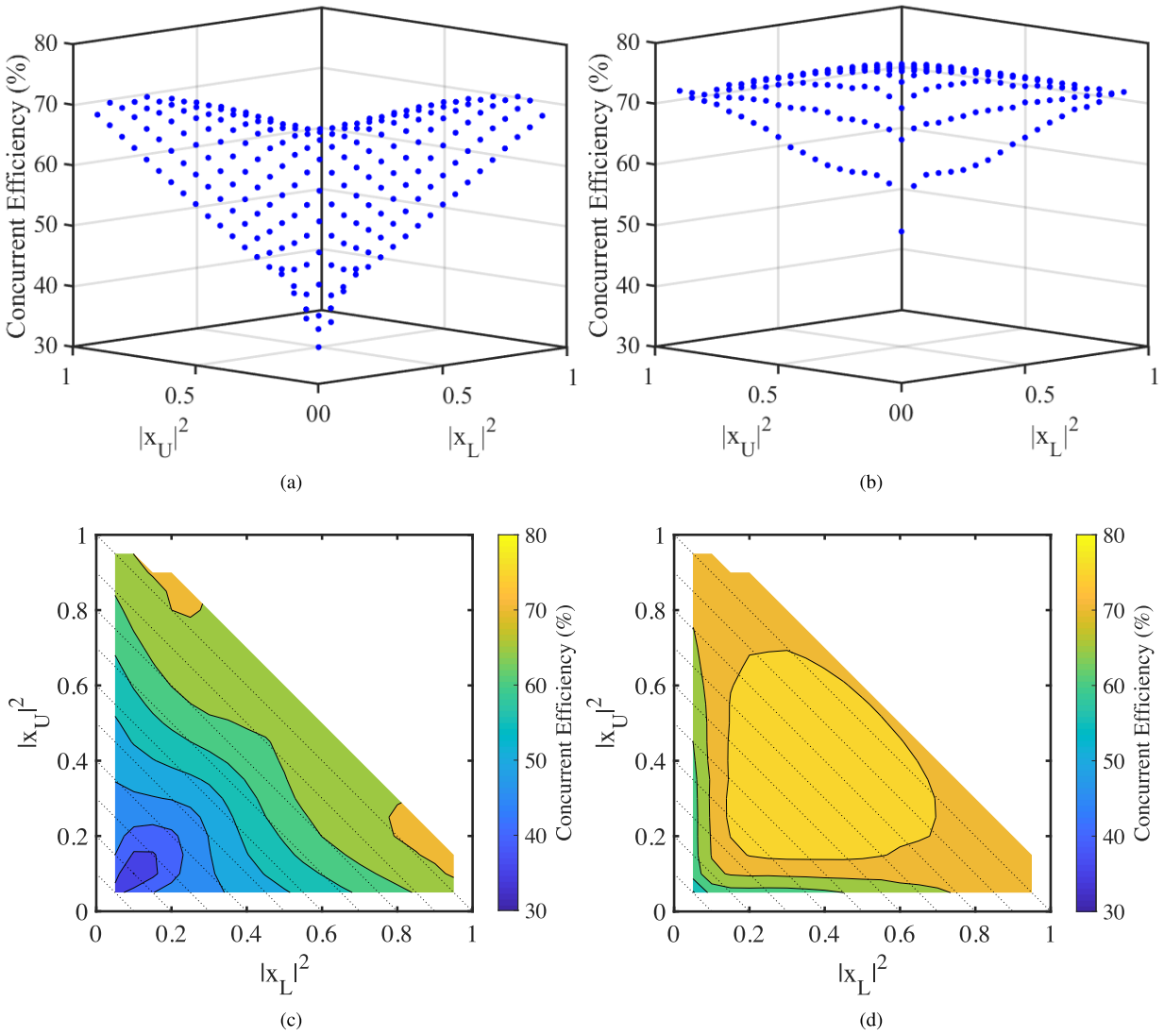

Fig. 16. (a) and (b) 3-D plot and (c) and (d) contour plot of the total drain efficiency versus normalized input powers $|x_L|^2$ and $|x_U|^2$ for the 2- and 3-Way DB-DPAs.

performance of the 2- and 3-Way DB-DPAs for dual-band modulated signals. The average concurrent efficiency for the 2-Way DB-DPA is 46.1%, while it is 61.2% for the 3-Way DB-DPA. This indicates that the 3-Way DB-DPA's architecture should provide a significant improvement in average efficiency compared to the conventionally 2-Way DB-DPA for concurrent dual-band operation.

To gain further insights in the origin of the efficiency improvement, a comparison of the drain efficiencies versus output power obtained for the 3-Way and 2-Way DB-DPAs is presented in Fig. 17 for the CB mode ($K = 1$). η(3W), η_m(3W), and η_a(3W) (red lines) represent the total, main, and auxiliary drain efficiencies in the 3-Way DB-DPA, respectively. η(2W), η_m(2W), and η_a(2W) (green lines) represent the total, main, and auxiliary drain efficiencies in the 2-Way DB-DPA, respectively. The total and partial efficiencies η, η_m, and η_a were defined themselves in Section III. The joint PDF of the two LTE uncorrelated signals with 6.27-dB PAPR is also plotted versus the output power with a blue line in Fig. 17 for the CB mode ($K = 1$). The joint PDF indicates that

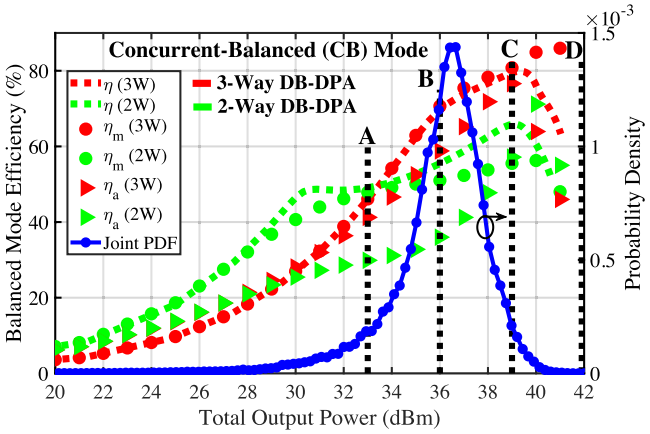

Fig. 17. Comparison of 3- and 2-Way DB-DPAs at the CSRP for the CB mode ($K = 1$).

the output power range where the PA operates most of the time corresponds to the power range where the total efficiency for the 3-Way DB-DPA (red line) is increased by 15 points

compared to the total efficiency of the traditional 2-Way DB-DPA (green line). The peak power at point C in the CB mode was targeted by the design theory to be 39 dBm. However, the efficiency of the 3-Way DB-DPA is found in simulation to remain high for an output power up to 41 dBm.

D. 3-Way DB-DPA at the Package Using Cree Model

After the design of the 3-Way DB-DPA at the CSRP is completed, the projected voltages and currents from the embedding model are used to construct the 3-Way DB-DPA at the PRP. The projected voltages and currents at the gate and drain of the transistors at the PRP provide the lossy two-port combiner at the fundamental frequency and the harmonic input and output impedances for both the main and auxiliary amplifiers.

First, based on the harmonic impedances obtained from the embedding model, the input second and output second- and third-harmonic termination networks for the three amplifiers were designed for both bands. In addition, for the dual-band auxiliary PA, termination networks are needed at the output for the second-order IM products. The termination network for the upper second-order IM product at $f_L + f_U$ is implemented together with the other harmonic termination networks. However, for the second-order IM product at $f_U - f_L$ that is at a lower frequency than the fundamental frequencies f_L and f_U, its impedance termination is implemented using a diplexer in combination with the drain bias tee. Two parallel dc capacitors (100 pF) are used after the harmonic termination network of each amplifier to isolate their respective dc supplies.

In the following step, the dual-band output combiner of the 3-Way DB-DPA is designed. The harmonic networks designed are first deembedded from the fundamental lossy two-port combiner at the PRP and implemented for both bands using two lossless two ports and a common output load. The resulting dual-band combiner terminated with the load and extended with the harmonic terminations is then optimized using electromagnetic (EM) simulations to approach the projected Y-parameters of the lossy two-port combiner obtained from the embedding model for each band at the PRP.

Finally, the input circuits were designed. Using the projected incident waves at the PRP from the embedding model, the WPD ratios at the PRP between the main and auxiliary PAs were determined and the WPD designed for each band. The WPD at f_L is designed using a resistor of 30.1 Ω, whereas the WPD at f_U uses a resistor of 49.9 Ω. Next, the input circuits of the 3-Way DB-DPA were designed and verified in ADS using EM models. This includes the *RC* networks close to the gate of the transistors that are used to stabilize the PA. The values for the resistor and capacitor are 150 Ω and 3.0 pF, respectively. The networks for the input second harmonic for the main and auxiliary amplifiers were designed. It was observed that the phase of the source reflection coefficient $\Gamma_S(2\omega_{U/L})$ has a strong impact on the main PAs' performance. Finally, conjugate input matching networks were then designed at the fundamental frequencies for the three amplifiers. Radial stubs were used in the design of all the input and output bias tees to precisely isolate the fundamental frequencies from the dc path.

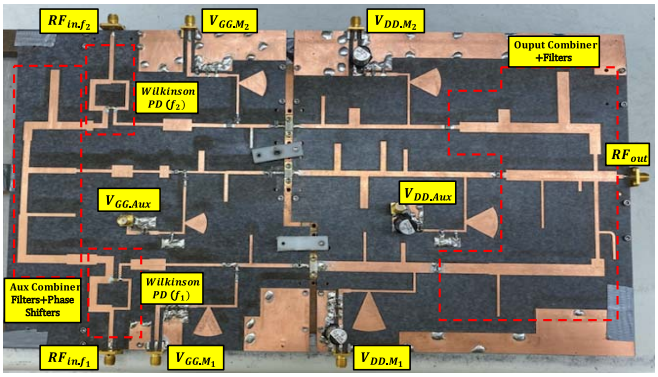

Fig. 18. 3-Way DB-DPA fabricated circuit.

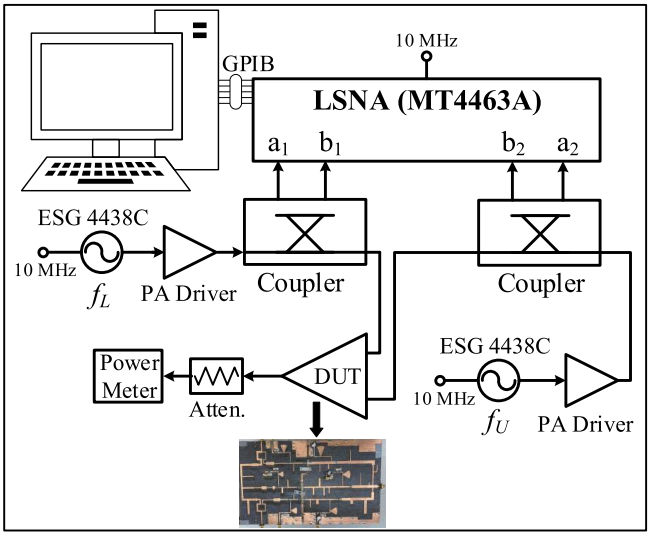

Fig. 19. LSNA test-bench used for the measurements for the SB and CB modes of operation.

Using all the above steps, the various components of the 3-Way DB-DPA shown in Fig. 1 were implemented. After combining all the subnetworks together, the performance of the 3-Way DB-DPA was verified using EM models (EM cosimulation). The fabricated 3-Way DB-DPA is shown in Fig. 18. The PA is built on a Rogers IsoClad 917 with a relative dielectric constant of 2.2 and a thickness of 31 mil. A Wolfspeed's GaN HEMT transistor (CHG40010F) is used for the three amplifiers. The final ADS momentum simulation results of the 3-Way DB-DPA will be compared with the CW measurements in Section IV.

IV. Measurement of the Novel 3-Way DB-DPA

A. CW Measurements

The new 3-Way DB-DPA was tested using a large-signal network analyzer (LSNA) for CW signals. The testbed setup of the LSNA measurement is shown in Fig. 19. The CW SB mode (nonconcurrent) measurements at f_L and f_U are shown in Fig. 20. They are based on the input power points (green circles) shown in Fig. 21.

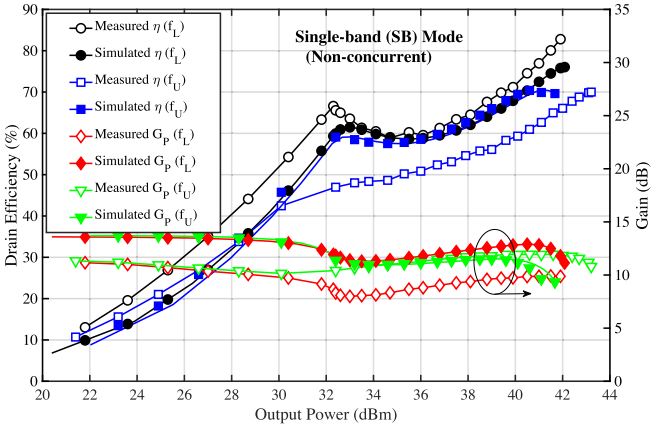

Fig. 20. CW simulations versus measurements at 1.5 and 2.0 GHz for the SB mode.

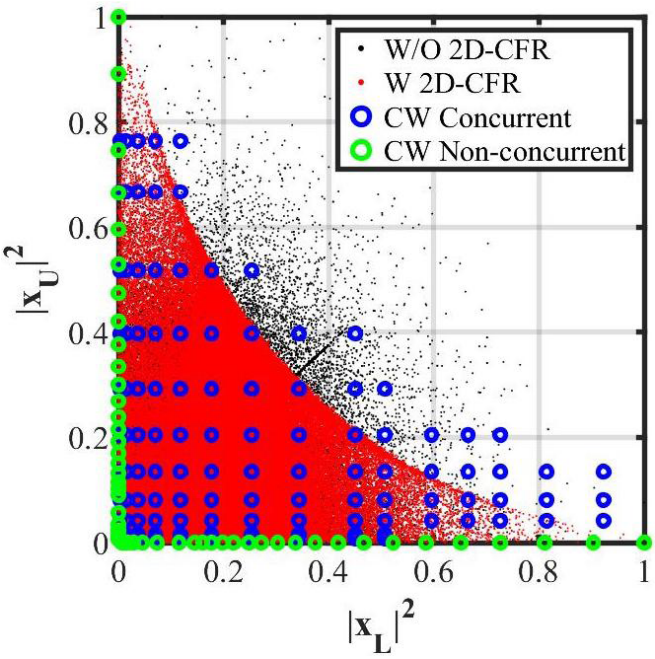

Fig. 21. 10-MHz LTE uncorrelated signals before 2-D CFR (black dots), after 2-D CFR (red dots), and CW measurements in an SB operation (green circles) and in concurrent operation (blue circles).

The measured CW SB efficiency at the lower band (1.5 GHz) shows a peak and backoff efficiencies of 82.8% and 66.6%, respectively. The OBO for the lower band is equal to 9.6 dB. The measured drain efficiency (black line with hollow circles) at the lower band has slightly better performance than the EM simulation efficiency result, which is shown using a black line with solid circles. The measured SB gain at f_L is around 10 dB.

The measured CW SB drain efficiency at the upper-band (2.0 GHz) is 70.0% at peak and 48.4% at backoff. Its OBO is equal to 9.4 dB. There is a degradation of the measured efficiency at backoff (blue line with hollow squares) compared to simulation (blue line with solid squares). This degradation is associated with the input second harmonic of the main amplifier at the upper-band. The measured phase of the input

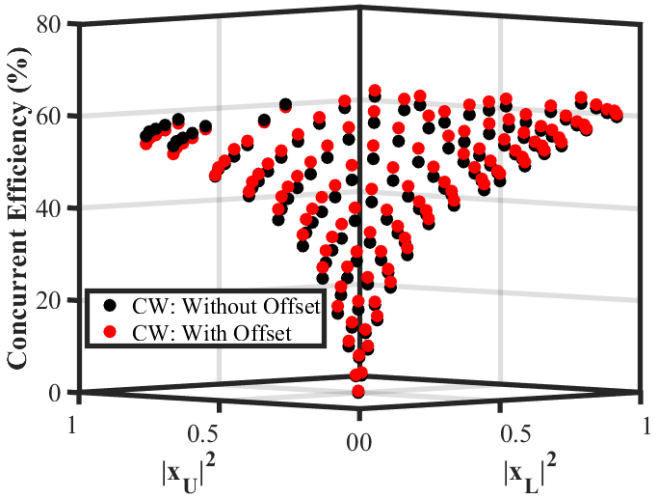

Fig. 22. CW measurements at 2.00 GHz (black circles) and at 2.01 GHz (red circles) with fixed 1.50 GHz for concurrent operation.

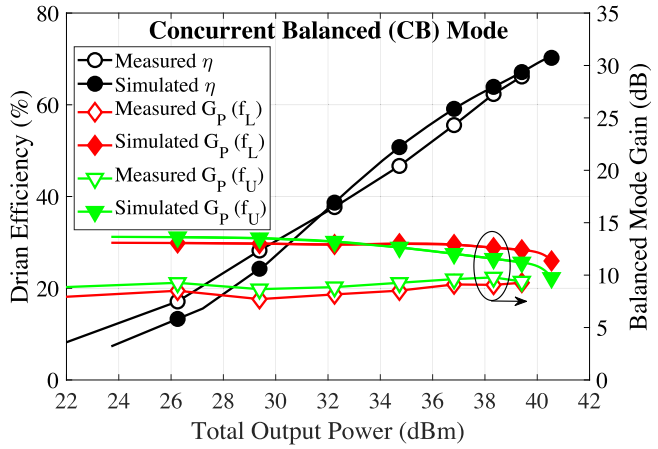

Fig. 23. CW simulations versus measurements for the CB mode.

second-harmonic reflection coefficient $\Gamma_S(f_U)$ was shifted to a lower value after fabrication. This was verified in a subsequent harmonic balance simulation to cause the 3-Way DB-DPA drain efficiency to degrade at backoff for the upper-band. The measured SB gain at f_U is around 11 dB.

For the CW concurrent mode evaluation of the 3-Way DB-DPA, 114 operating points with different amplitude ratio K between the two input RF signals were selected in the $(|x_L|^2, |x_U|^2)$ power space as shown in Fig. 21 using blue circles. The results for the CW concurrent total efficiency for these 114 dual-band operating points at 1.50 and 2.00 GHz are shown in black filled circles in Fig. 22.

To test the phase independence of the CW performance of the 3-Way DB-DPA, the upper band is set to 2.01 GHz instead of 2.00 GHz. Note that for this 10-MHz frequency shift, the greatest common divider between f_L and f_U is now 30 MHz instead of 500 MHz. The results for the CW concurrent efficiency when using 2.01 and 1.50 GHz are shown in red-filled circles in Fig. 22. Note that shifting the upper frequency by 10 MHz is equivalent to sweeping the phase of x_U from 0 to 2π over a period of 0.1 μs. The similarity between the concurrent responses for 2 GHz (black)

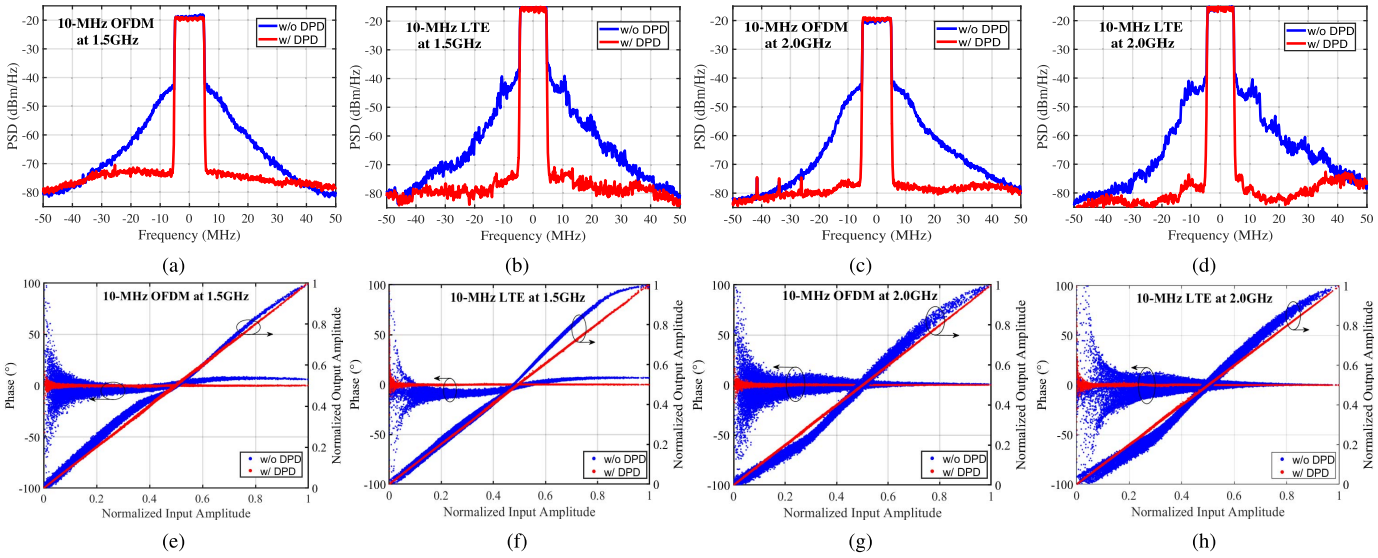

Fig. 24. SB output-power spectral density and AM/AM and AM/PM before (blue) and after (red) DPD for (a) and (e) 10-MHz OFDM at 1.5 GHz, (b) and (f) 10-MHz LTE at 1.5 GHz, (c) and (g) 10-MHz OFDM at 2.0 GHz, and (d) and (h) 10-MHz LTE at 2.0 GHz.

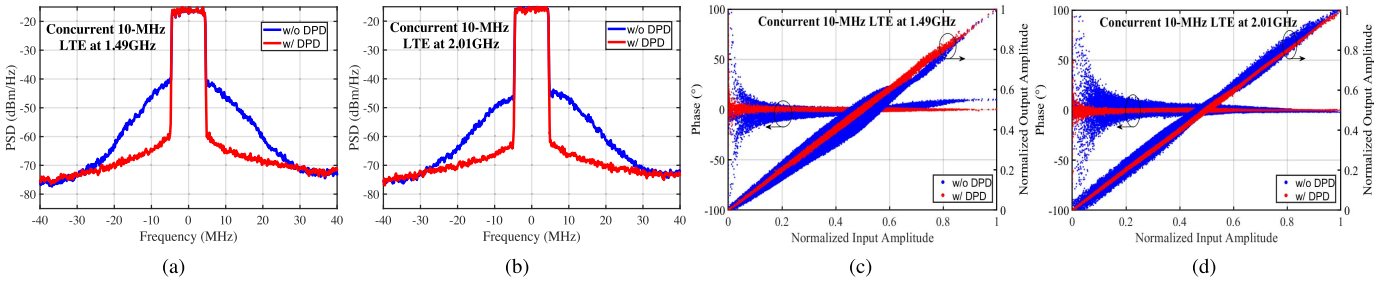

Fig. 25. Concurrent output-power spectral density and AM/AM and AM/PM before (blue) and after (red) DPD, for two uncorrelated 10-MHz LTE signals. (a) and (c) 6.86-dB PAPR at 1.49 GHz. (b) and (d) 6.27-dB PAPR at 2.01 GHz.

and 2.01 GHz (red) demonstrates the independence of the CW performance of the 3-Way DB-DPA to the relative phase between the CW excitation. Nevertheless, the CW concurrent performance of the PA in CB mode exhibits a slightly better efficiency at 2.01 GHz than 2.0 GHz. This is verified in Fig. 23 where the measured peak efficiency in the CW CB ($K = 1$) mode is seen to reach 66.2% at 2.01 GHz. This shows that the 3-Way DB-DPA overcomes the limitation of the conventional topology in the DB-DPA. Note that the measured CB mode drain efficiency (black line with hollow circles) is very close to the EM simulation results (black line with solid circles) in Fig. 23, despite the degradation in the upper band in the SB mode.

The measured CB mode power gains at 1.5 and 2.0 GHz are also shown in Fig. 23 for CW excitations. The measured power gain in the CB mode is degraded by about 3 dB in average compared to the simulated power gains. This degradation is believed to originate from both fabrication issues as well as limitations in the GaN HEMT model accuracy.

B. SB and Concurrent Modulated Signal Measurements With 2-D CFR

The 3-Way DB-DPA was tested using modulated signals in both the SB and concurrent modes of operation. The output power spectral density and AM/AM and AM/PM before (blue) and after (red) digital predistortion (DPD) are shown in Fig. 24 for the SB mode and in Fig. 25 for the concurrent mode.

For the SB mode, a 10-MHz OFDM signal with 9.5-dB PAPR was injected at 1.5 GHz, and the DPD results are shown in Fig. 24(a) and (e). The average power and drain efficiency before DPD are 31.8 dBm and 53.3%, respectively. After DPD, the average power and drain efficiency are 31.2 dBm and 50.4%, respectively. A 10-MHz LTE signal with 6.1-dB PAPR was also injected at f_L, and the DPD results are shown in Fig. 24(b) and (f). The average power and drain efficiency at 1.5 GHz before DPD are 35.9 dBm and 68.4%, respectively. After DPD, the average power and efficiency are 35.1 dBm and 65.0%, respectively. The same signals are applied for the upper band (2.0 GHz) in the SB mode. The DPD results at the 2.0 GHz when using 10-MHz OFDM signal with 9.5-dB PAPR are shown in Fig. 24(c) and (g). The average power and efficiency before DPD are 32.9 dBm and 41.4%, respectively. After DPD, the average power and efficiency are 33.4 dBm and 41.2%, respectively. Similarly, a 10-MHz LTE signal with 6.1-dB PAPR is injected at 2.0 GHz. The DPD results are shown in Fig. 24(d) and (h). The average power and drain efficiency before DPD are 37.5 dBm and 55.3%, while the results after DPD are 37.4 dBm and 53.7%, respectively. A summary of the modulated signal results in the SB mode is shown in Table IV. For the concurrent mode, two uncorrelated

TABLE IV
SB MODE MODULATED SIGNAL MEASUREMENTS

	f_0 (GHz)	Signal	Output PAPR (dB)	$P_{out,avg.}$ (dBm)	$\eta_{DE,avg.}$ (%)	$ACLR_{L,H}$ (dBc)	NMSE (dB)
Before DPD	1.5	10-MHz OFDM	8.9	31.8	53.3	$-28.0, -27.8$	-18.2
After DPD	1.5	10-MHz OFDM	9.5	31.2	50.4	$-53.6, -53.8$	-42.9
Before DPD	1.5	10-MHz LTE	5.5	35.9	68.4	$-29.2, -28.8$	-18.3
After DPD	1.5	10-MHz LTE	6.1	35.1	65.0	$-60.4, -58.7$	-40.6
Before DPD	2.0	10-MHz OFDM	10.0	32.9	41.4	$-26.7, -25.6$	-17.8
After DPD	2.0	10-MHz OFDM	9.5	33.4	41.2	$-57.6, -57.9$	-45.5
Before DPD	2.0	10-MHz LTE	5.9	37.5	55.3	$-29.1, -29.9$	-22.3
After DPD	2.0	10-MHz LTE	6.1	37.4	53.7	$-62.3, -62.6$	-49.2

TABLE V
CONCURRENT MODE MODULATED SIGNAL MEASUREMENTS

	f_0 (GHz)	Signal	Output PAPR (dB)	$P_{out.avg}$ (dBm)	$\eta_{DE.tot.avg.}$ (%)	$ACLR_{L,H}$ (dBc)	NMSE (dB)
Before DPD	1.49	10-MHz LTE	6.9	34.8	–	$-28.8, -28.8$	-21.2
After DPD	1.49	10-MHz LTE	6.8	35.4	–	$-47.3, -47.3$	-35.0
Before DPD	2.01	10-MHz LTE	6.0	35.5	–	$-34.2, -31.6$	-23.9
After DPD	2.01	10-MHz LTE	6.3	34.4	–	$-49.8, -49.5$	-38.2
Before DPD	1.49+2.01	10-MHz LTE	–	37.7	55.2	–	–
After DPD	1.49+2.01	10-MHz LTE	–	37.5	54.2	–	–

TABLE VI
COMPARISON WITH RECENT DUAL-BAND DOHERTY PAS

Technology	Signal	PAPR (dB)	Frequency (GHz)	$P_{out.avg}(total)$ (dBm)	$\eta_{DE.tot.avg.}$ (%)	ACPR (dBc)	Reference
15-W GaN	5-MHz WCDMA/10-MHz LTE	7/7	1.8/2.4	36.2/36.1 (33.3)	35.6	-55.1/-50.5	[25]
10-W GaN	10-MHz LTE/15-MHz LTE	7.5/7.5	0.85/2.33	- (31.75)	26.7	-47.1/-49.4	[15]
25-W GaN	20-MHz LTE/20-MHz LTE	7.2/7.2	2.15/3.4	39.5/39.1 (37.1)	34.8	-50/-47.8	[11]
10-W GaN	10-MHz LTE/10-MHz LTE	7/7	1.9/2.6	35.14/34.82 (38.01)	46.6	-45.6/-45.1	[18]
6-W GaN	10-MHz LTE/10-MHz LTE	6/6	3.5/5.5	29.03/38.13 (-)	29.5	-46.8/-48.0	[26]
6-W GaN	5-MHz WCDMA/5-MHz WCDMA	9/9	1.4/3.5	32.5/32.5 (-)	52.1/51.3 (-)	-33.1/-25.3	[27]
25-W GaN	20-MHz WCDMA/20-MHz LTE	9.6	2.1/3.45	- (37.9)	37.5	-45.9/-47.3	[28]
10-W GaN	10-MHz LTE/10-MHz LTE	6.8/6.3	1.5/2.0	35.4/34.4 (37.5)	54.2	-47.3/-49.5	**This work**

10-MHz LTE signals are used. Their associated 2-D power distribution is shown using black dots in Fig. 21. In order to avoid hard clipping in the auxiliary PA of the 3-Way DB-DPA, a 2-D CFR technique similar to the ones reported in [18] and [24] was used. The following equation was used for the 2-D CFR:

$$x'_{L/U}(n) = \begin{cases} \dfrac{x_{L/U}(n)}{T} & \text{if } |x_L| + |x_U| \le T \\ x_{L/U}(n) \times \dfrac{1}{|x_L| + |x_U|} & \text{if } |x_L| + |x_U| > T \end{cases}$$

where T represents the clipping threshold of the 2-D signals at which the 2-D CFR is applied. $T = 0.9220$ was used in this work. After using the 2-D CFR, a spectral regrowth is observed. A cascade of finite impulse response (FIR) filtering was used to remove the spectral regrowth in order to increase the dynamic range after the 2-D CFR. The final 2-D signals plotted in the $(|x_L|^2, |x_U|^2)$ space before the injection are shown with red dots in Fig. 21. After 2-D CFR, the final PAPRs are 6.86 dB at 1.49 GHz and 6.27 dB at 2.01 GHz.

These dual-band signals were injected concurrently at the inputs of the new 3-Way DB-DPA. Note that lower and upper frequencies of 1.49 and 2.01 GHz were selected so that the even-order IM products are not located in bands. The output power spectral density and AM/AM and AM/PM before (blue) and after (red) DPD are shown in Fig. 25(a) and (c) for 1.49 GHz and Fig. 25(b) and (d) for 2.01 GHz. The average total powers and average concurrent efficiencies before and after DPD are 37.7/37.5 dBm and 55.2/54.2%, respectively. A summary of the concurrent modulated signal results is given in Table V. Finally, a comparison of the results obtained with the new 3-Way DB-DPA with published results is given in Table VI for similar devices. Given that the comparison is for relatively similar LTE signals in terms of frequencies, bandwidth, and PAPR, the new 3-Way DB-DPA exhibits

a significantly larger concurrent power efficiency compared to other 2-Way DB-DPAs while providing a reasonable output power.

V. Conclusion

A novel 3-Way DB-DPA has been designed at 1.5 and 2.0 GHz. This new dual-band PA consists of two main amplifiers to handle each band individually and a single auxiliary amplifier that is shared by both bands. A preliminary analysis of clipping, phase, and IM effects on the 3-Way DB-DPA has been performed to guide the design. A comprehensive theory and design methodology was developed and reported for the 3-Way DB-DPA. Essentially by using two main amplifiers, early clipping in concurrent dual-band operation is avoided, allowing for both of the main amplifiers to benefit from load—pulling from the auxiliary amplifier. Furthermore, to make the SB operation compatible with the concurrent dual-band operation, the voltage saturation in the main amplifier in SB operation is first achieved by clipping for gate drives between the CB backoff ($V_{\mathrm{GS,mb1}}$) and SB backoff ($V_{\mathrm{GS,mb2}}$) before load—pulling takes over. The 3-Way DB-DPA using two main amplifiers achieves a higher concurrent efficiency compared to the conventional 2-Way DB-DPA. This has been verified by a theoretical analysis and a statistical analysis using CW simulations and validated in measurements. The 3-Way DB-DPA was implemented and fabricated, and it was experimentally evaluated using both CW and modulated signals. The 3-Way DB-DPA achieved in measurement a concurrent average efficiency of 54.2% and an average total power of 37.5 dBm after DPD, which corresponds to a significant improvement on previously reported Doherty PAs designed for dual-band concurrent operation. To the best of the authors' knowledge, this is the first 3-Way DB-DPA that features two main amplifiers and a single auxiliary amplifier.

Acknowledgment

The Ohio State University would like to acknowledge the donation by Texas Instruments of the RF-ADC and RF-DAC testbed used in the DPD linearization work. The authors would like to thank Rogers Corporation for the donation of the Duroid substrate.

References

[1] W. H. Doherty, "A new high efficiency power amplifier for modulated waves," *Proc. IRE*, vol. 24, no. 9, pp. 1163–1182, Sep. 1936.

[2] F. Raab, "Efficiency of Doherty RF power-amplifier systems," *IEEE Trans. Broadcast.*, vol. BC-33, no. 3, pp. 77–83, Sep. 1987.

[3] B. Kim, J. Kim, I. Kim, and J. Cha, "The Doherty power amplifier," *IEEE Microw. Mag.*, vol. 7, no. 5, pp. 42–50, Oct. 2006.

[4] J. Kim, "Highly efficient asymmetric class-F^{-1}/F GaN Doherty amplifier," *IEEE Trans. Microw. Theory Techn.*, vol. 66, no. 9, pp. 4070–4077, Sep. 2018.

[5] H. Jang, P. Roblin, C. Quindroit, Y. Lin, and R. D. Pond, "Asymmetric Doherty power amplifier designed using model-based nonlinear embedding," *IEEE Trans. Microw. Theory Techn.*, vol. 62, no. 12, pp. 3436–3451, Dec. 2014.

[6] C. Liang, P. Roblin, and Y. Hahn, "Accelerated design methodology for dual-input Doherty power amplifiers," *IEEE Trans. Microw. Theory Techn.*, vol. 67, no. 10, pp. 3983–3995, Oct. 2019.

[7] M. Ozen, K. Andersson, and C. Fager, "Symmetrical Doherty power amplifier with extended efficiency range," *IEEE Trans. Microw. Theory Techn.*, vol. 64, no. 4, pp. 1273–1284, Apr. 2016.

[8] P. Colantonio, F. Feudo, F. Giannini, R. Giofrè, and L. Piazzon, "Design of a dual-band GaN Doherty amplifier," in *Proc. 18th Int. Microw. Radar Wireless Commun. Conf.*, Jun. 2010, pp. 1–4.

[9] W. Chen *et al.*, "Design and linearization of concurrent dual-band Doherty power amplifier with frequency-dependent power ranges," *IEEE Trans. Microw. Theory Techn.*, vol. 59, no. 10, pp. 2537–2546, Oct. 2011.

[10] Z. Yang, M. Li, Y. Yao, Z. Dai, T. Li, and Y. Jin, "Design of concurrent dual-band continuous class-J mode Doherty power amplifier with precise impedance terminations," *IEEE Microw. Wireless Compon. Lett.*, vol. 29, no. 5, pp. 348–350, May 2019.

[11] M. Liu, H. Golestaneh, and S. Boumaiza, "A concurrent 2.15/3.4 GHz dual-band Doherty power amplifier with extended fractional bandwidth," in *IEEE MTT-S Int. Microw. Symp. Dig.*, May 2016, pp. 1–3.

[12] X. Li, W. Chen, Z. Zhang, Z. Feng, X. Tang, and K. Mouthaan, "A concurrent dual-band Doherty power amplifier," in *Proc. Asia–Pacific Microw. Conf.*, Dec. 2010, pp. 654–657.

[13] X. Chen, W. Chen, G. Su, F. M. Ghannouchi, and Z. Feng, "A concurrent dual-band 1.9–2.6-GHz Doherty power amplifier with intermodulation impedance tuning," in *IEEE MTT-S Int. Microw. Symp. Dig.*, Jun. 2014, pp. 1–4.

[14] P. Saad, R. Hou, R. Hellberg, and B. Berglund, "A 1.8–3.8-GHz power amplifier with 40% efficiency at 8-dB power back-off," *IEEE Trans. Microw. Theory Techn.*, vol. 66, no. 11, pp. 4870–4882, Nov. 2018.

[15] W. Chen, S. Zhang, Y. Liu, Y. Liu, and F. M. Ghannouchi, "A concurrent dual-band uneven Doherty power amplifier with frequency-dependent input power division," *IEEE Trans. Circuits Syst. I, Reg. Papers*, vol. 61, no. 2, pp. 552–561, Feb. 2014.

[16] A. Barthwal, G. Ajmera, K. Rawat, A. Basu, and S. K. Koul, "Design scheme for dual-band three stage Doherty power amplifiers," in *Proc. IEEE Int. Microw. RF Conf. (IMaRC)*, Dec. 2014, pp. 80–83.

[17] J. Pang, S. He, Z. Dai, C. Huang, J. Peng, and F. You, "Novel design of highly-efficient concurrent dual-band GaN Doherty power amplifier using direct-matching impedance transformers," in *IEEE MTT-S Int. Microw. Symp. Dig.*, May 2016, pp. 1–4.

[18] X. Chen, W. Chen, F. Huang, F. M. Ghannouchi, Z. Feng, and Y. Liu, "Systematic crest factor reduction and efficiency enhancement of dual-band power amplifier based transmitters," *IEEE Trans. Broadcast.*, vol. 63, no. 1, pp. 111–122, Mar. 2017.

[19] M. R. Duffy, G. Lasser, M. Olavsbraten, E. Berry, and Z. Popovic, "Efficient multisignal 2–4-GHz power amplifier with power tracking," *IEEE Trans. Microw. Theory Techn.*, vol. 66, no. 12, pp. 5652–5663, Dec. 2018.

[20] D. J. Shepphard, J. Powell, and S. C. Cripps, "An efficient broadband reconfigurable power amplifier using active load modulation," *IEEE Microw. Wireless Compon. Lett.*, vol. 26, no. 6, pp. 443–445, Jun. 2016.

[21] H. Jang, P. Roblin, and C. Quindroit, "Adjustable load-modulation asymmetric Doherty amplifier design using nonlinear embedding," in *IEEE MTT-S Int. Microw. Symp. Dig.*, Jun. 2014, pp. 1–4.

[22] C. Liang, P. Roblin, Y. Hahn, Z. Popovic, and H.-C. Chang, "Novel outphasing power amplifiers designed with an analytic generalized Doherty–Chireix continuum theory," *IEEE Trans. Circuits Syst. I, Reg. Papers*, vol. 66, no. 8, pp. 2935–2948, Aug. 2019.

[23] H. Jang, P. Roblin, and Z. Xie, "Model-based nonlinear embedding for power-amplifier design," *IEEE Trans. Microw. Theory Techn.*, vol. 62, no. 9, pp. 1986–2002, Sep. 2014.

[24] X. Chen, S. Zhang, and W. Chen, "Two-dimensional crest factor reduction for performance improvement of concurrent dual-band power amplifiers," *Electron. Lett.*, vol. 49, no. 18, pp. 1163–1165, Aug. 2013.

[25] P. Saad, P. Colantonio, L. Piazzon, F. Giannini, K. Andersson, and C. Fager, "Design of a concurrent dual-band 1.8–2.4-GHz GaN-HEMT Doherty power amplifier," *IEEE Trans. Microw. Theory Techn.*, vol. 60, no. 6, pp. 1840–1849, Jun. 2012.

[26] T. Cappello, A. Duh, T. W. Barton, and Z. Popovic, "A dual-band dual-output power amplifier for carrier aggregation," *IEEE Trans. Microw. Theory Techn.*, vol. 67, no. 7, pp. 3134–3146, Jul. 2019.

[27] H.-Y. Liu, C. Zhai, and K.-K.-M. Cheng, "Novel dual-band equal-cell Doherty amplifier design with extended power back-off range," *IEEE Trans. Microw. Theory Techn.*, vol. 68, no. 3, pp. 1012–1021, Mar. 2020.

[28] M. Liu, X. Fang, H. Huang, and S. Boumaiza, "Dual-band 3-way Doherty power amplifier with extended back-off power and bandwidth," *IEEE Trans. Circuits Syst. II, Exp. Briefs*, vol. 67, no. 2, pp. 270–274, Feb. 2020.

Ruwaybih Alsulami (Student Member, IEEE) was born in Mecca, Saudi Arabia. He received the B.S. degree in electrical and computer engineering from the University of Colorado at Boulder, Boulder, CO, USA, in 2011, the M.S. degree in electrical engineering from the University of Colorado at Colorado Springs, Colorado Springs, CO, USA, in 2013, and the M.S. and Ph.D. degrees in electrical and computer engineering from The Ohio State University, Columbus, OH, USA, in 2020 and 2021, respectively.

He is currently an Assistant Professor of electrical engineering with Umm Al Qura University, Mecca. His current research interests include multiband Doherty power amplifiers' design, linearization, and measurements of nonlinear microwave devices and circuits.

Patrick Roblin (Senior Member, IEEE) received the Maitrise de Physics degree from Louis Pasteur University, Strasbourg, France, in 1980, and the M.S. and D.Sc. degrees in electrical engineering from Washington University, St. Louis, MO, USA, in 1982 and 1984, respectively.

In 1984, he joined the Department of Electrical Engineering, The Ohio State University (OSU), Columbus, OH, USA, as an Assistant Professor, where he is currently a Professor. He is the Founder of the Non-Linear RF Research Laboratory, OSU. He is the lead author of the two textbooks: *High-Speed Heterostructure and Devices* (Cambridge University Press, 2002) and *Nonlinear RF Circuits and Nonlinear Vector Network Analyzers* (Cambridge University Press, 2011). His current research interests include the measurement, modeling, design, and linearization of nonlinear RF devices and circuits, such as oscillators, mixers, and power amplifiers.

Dr. Roblin served as a distinguished microwave lecturer from 2016 to 2018.

Jose I. Martinez-Lopez (Member, IEEE) was born in Mexico City, Mexico. He received the B.S., M.Eng., and Ph.D. degrees in electrical engineering from the National Autonomous University of Mexico (UNAM), Mexico City, in 1994, 1998, and 2005, respectively.

In 2006, he was with the Schlumberger Technology Center, Sugar Land, TX, USA, where he was developing antennas for deep induction array tools for the oil industry. In 2009, he was a Visiting Scholar with the Electroscience Laboratory, The Ohio State University (OSU), Columbus, OH, USA. He is currently a Professor of electrical engineering with UNAM. At present, he is on a sabbatical leave as a Visiting Scholar at the Nonlinear RF Laboratory, Department of Electrical and Computer Engineering, OSU. His current research interests include antenna arrays, frequency-selective surfaces, and microwave and millimeter-wave circuits.

Yunsik Hahn (Student Member, IEEE) is currently pursuing the Ph.D. degree in electrical and computer engineering at The Ohio State University, Columbus, OH, USA.

His main research interest is the linearization of RF nonlinear power amplifiers and multi-input–multioutput (MIMO) transmitters with digital predistortion (DPD) techniques for future wireless communication systems.

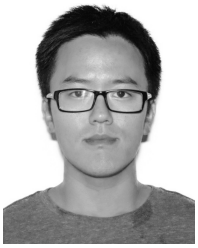

Chenyu Liang (Member, IEEE) received the B.S. degree in electrical and computer engineering from New Mexico State University, Las Cruces, NM, USA, in 2013, the B.Eng. degree in electrical engineering from the University of Electronic Science and Technology of China (UESTC), Chengdu, China, in 2013, and the M.S. and Ph.D. degrees in electrical and computer engineering from The Ohio State University, Columbus, OH, USA, in 2016 and 2020, respectively.

Since 2020, he has been a Senior Design Engineer with Qorvo, San Jose, CA, USA, where he is currently involved with the RF/mmWave IC front-end module and power amplifiers design. His main research interests include sub-6-GHz high-efficiency wideband Doherty power amplifiers for base-station applications, RF/millimeter-wave IC power amplifier design, and nonlinear RF measurement using a nonlinear vector network analyzer.

Dr. Liang was a recipient of the 2019 Fall Outstanding Teaching Assistant Award of the Department of Electrical and Computer Engineering, The Ohio State University.

Zoya Popovic (Fellow, IEEE) received the Dipl.Ing. degree from the University of Belgrade, Belgrade, Serbia, in 1985, and the Ph.D. degree from Caltech, Pasadena, CA, USA, in 1990.

She is currently a Distinguished Professor and the Lockheed Martin Endowed Chair of Electrical Engineering at the University of Colorado at Boulder, Boulder, CO, USA. From 2001 to 2003, she was a Visiting Professor with the Technical University of Munich, Munich, Germany. In 2014, she was a Visiting Professor with the Institut Supérieur De L'aéronautique Et De L'espace (ISAE), Toulouse, France. She has graduated 56 Ph.D. students and currently advises 12 doctoral students. Her research interests are in high-efficiency power amplifiers and transmitters, microwave and millimeter-wave high-performance circuits for communications and radar, medical applications of microwaves, millimeter-wave, and THz quasi-optical techniques, and wireless powering.

Dr. Popovic was a recipient of two IEEE MTT Microwave Prizes for best journal articles, the White House NSF Presidential Faculty Fellow Award, the URSI Issac Koga Gold Medal, the ASEE/HP Terman Medal, and the German Humboldt Research Award. She was elected as a Foreign Member of the Serbian Academy of Sciences and Arts in 2006. She was named an IEEE MTT Distinguished Educator in 2013 and the University of Colorado Distinguished Research Lecturer in 2015.

Vanessa Chen (Member, IEEE) received the Ph.D. degree in electrical and computer engineering from Carnegie Mellon University, Pittsburgh, PA, USA, in 2013.

She was with Qualcomm, San Diego, CA, USA, where she worked on energy-efficient data-acquisition systems for mobile devices. She was an Assistant Professor at The Ohio State University, Columbus, OH, USA. From 2010 to 2013, at Carnegie Mellon University, she focused her research on self-healing systems and high-speed analog-to-digital converters (ADCs). She held a research internship position at the IBM T. J. Watson Research Center, Yorktown Heights, in 2012. She is currently an Assistant Professor of electrical and computer engineering at Carnegie Mellon University. Her research interests focus on data conversion interfaces for machine learning, RF/analog hardware security, ubiquitous sensing, and communication systems.

Dr. Chen is also a Technical Program Committee Member of the IEEE Custom Integrated Circuits Conference (CICC) and the IEEE Asian Solid-State Circuits Conference (A-SSCC). She was a recipient of the NSF CAREER Award in 2019, the Analog Devices Outstanding Student Designer Award in 2013, and the IBM Ph.D. Fellowship in 2012. She is also an Associate Editor of the IEEE OPEN JOURNAL OF CIRCUITS AND SYSTEMS.